Heidi E. O'Hora

Clumped-isotope-derived climate trends leading up to the end-Cretaceous mass extinction in northwest Europe

submitted in partial fulfillment of the requirements for the degree of
Master of Science in Earth and Environmental Sciences
Department of Earth and Environmental Sciences
The University of Michigan

	Accepted by:	
Siena Petersen	Sierra V. Petersen	7/2/21
Signature	Name	Date
[signature]	Benjamin H. Passey	7/2/21
	Name	Date
[signature]	Marin K. Clark	7/20/21
Department Chair Signature	Name	Date

I hereby grant the University of Michigan, its heirs and assigns, the non-exclusive right to reproduce and distribute single copies of my thesis, in whole or in part, in any format. I represent and warrant to the University of Michigan that the thesis is an original work, does not infringe or violate any rights of others, and that I make these grants as the sole owner of the rights to my thesis. I understand that I will not receive royalties for any reproduction of this thesis.

☑ Permission granted.

☐ Permission granted to copy after: _____

☐ Permission declined.
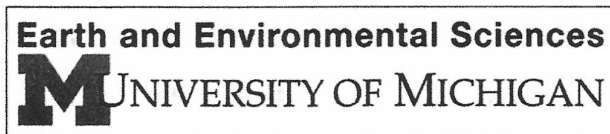
[signature]

Author Signature

Earth and Environmental Sciences
MUNIVERSITY OF MICHIGAN

TABLE OF CONTENTS

Abstract. Paleotemperature reconstructions linked to Deccan traps volcanic greenhouse gas emissions and associated feedbacks in the lead-up to the end-Cretaceous meteorite impact and extinction document local and global climate trends during a key interval of geologic history. Here, we present a new clumped-isotope-based paleotemperature record derived from fossil bivalves from the Maastrichtian type region, in southeast Netherlands and northeast Belgium. Clumped isotope data documents a mean temperature of 19.2 ± 3.8 °C, consistent with other Maastrichtian temperature estimates, and an average seawater $\delta^{18}O$ value of -0.2 ± 0.9‰ VSMOW for the region during the latest Cretaceous (67.1–66.0 Ma). A notable temperature increase at ~66.4 Ma is interpreted to be a regional manifestation of the globally-defined Late Maastrichtian Warming Event, linking Deccan Traps volcanic CO_2 emissions prior to the end-Cretaceous extinction to climate change in the Maastricht region. Fluctuating seawater $\delta^{18}O$ values coinciding with temperature changes suggest alternating influences of warm, salty southern-sourced waters and cooler, fresher northern-sourced waters from the Arctic Ocean. This new paleotemperature record contributes to the understanding of regional and global climate response to large-scale volcanism and ocean circulation changes leading up to a catastrophic mass extinction.

1. INTRODUCTION

During the Late Maastrichtian, greenhouse gas emissions from the emplacement of the vast Deccan Traps large igneous province (LIP) on the Indian subcontinent resulted in global warming (see Hull et al., 2020 and references therein). This warming event (termed the Late Maastrichtian Warm Event or LMWE; Woelders et al., 2018) has been observed in multiple locations and has been dated to approximately coincide with the onset of major Deccan volcanism (66.413 ± 0.067 Ma; Sprain et al., 2019). Anomalous mercury concentrations in sediments (e.g., Font et al., 2016; Sial et al., 2016; Percival et al., 2018; Zhao et al., 2021) and fossil shells (Meyer et al., 2019) link the warming to a volcanic source, and modeling of the climate impacts of hypothesized volcanic CO_2 and Hg emissions result in warming consistent with observations (Tobin et al., 2017; Fendley et al., 2019; Nava et al., 2021).

Prior to the LMWE, global climate was in a "cool greenhouse" state (Scotese, 2021), with a small ice cap possible in Antarctica as indicated by models (Miller et al., 2005; Ladant and Donnadieu, 2016), sea-ice-indicating dinoflagellate cysts (Bowman et al., 2013), and coastal Antarctic temperatures near the freezing point (Petersen et al., 2016a). The LMWE may have caused these ice caps to melt (Bowman et al., 2013; Petersen et al, 2016a) and, subsequently, global sea level to rise. This is potentially visible in the global sea level curve of Haq (2014), but the resolution of this sea level record is too coarse to directly link cycles to the short-term LMWE.

After the LMWE, climate cooled again gradually, potentially due to silicate weathering feedbacks (Petersen et al., 2016a; Tobin et al., 2017), before being thrown into upheaval by the arrival of the Chicxulub meteorite impact, defining the Cretaceous-Paleogene (K-Pg) boundary (Molina et al., 2006). Ejecta from the impact covered the planet and resulted in a short-lived "impact winter" event (Vellekoop et al., 2014; Vellekoop et al., 2016). Taken together, Deccan Traps volcanism

and associated feedbacks and the Chicxulub bolide impact create a complex record of paleoenvironmental disturbances through the end-Cretaceous, ultimately leading to the rapid extinction of ~70 % of species on Earth (Schulte et al., 2010).

Previous studies have reconstructed Maastrichtian marine temperatures at sites around the globe using several different proxies including $\delta^{18}O$ of foraminifera, molluscs, tooth enamel, and bulk carbonate material (e.g., Pucéat et al., 2007; Tobin et al., 2012; Hull et al., 2020), TEX_{86} measurements (e.g., Vellekoop et al., 2016; Woelders et al., 2017), Mg/Ca ratios (e.g., Woelders et al., 2018), and clumped isotope thermometry (Dennis et al., 2013; Tobin et al., 2014; Petersen et al., 2016a; Petersen et al., 2016b, Meyer et al., 2018; Zhang et al., 2018; Meyer et al., 2019; Tagliavento et al., 2019) (Table A1). Taken together, these records clearly show a late Maastrichtian warming. However, at any given site, local ocean temperatures are influenced not only by global trends, but by local changes in ocean circulation, sea level, upwelling, runoff, etc. (changes which may themselves by driven indirectly by global climate change, e.g., sea level rise due to melting of the Antarctic ice caps during the LWME). Therefore, it is important to consider the local paleogeographic context when interpreting paleoclimate trends during this tumultuous period.

Here, we produce a new climate record for a site in northwest Europe using the clumped and stable isotopic composition of bivalve fossils to better constrain the magnitude of climate change and possible ocean circulation fluctuations during this key geologic transition interval. We focus on the Maastrichtian type area (Jagt and Jagt-Yazykova, 2012) in the Belgium-Netherlands border region near Maastricht, Netherlands. The reconstructed paleogeography of this locality—a shallow epicontinental sea surrounded by several low-lying landmasses (Fig. 1a)—makes this site sensitive not only to global climate changes, but to local variations in sea level and ocean circulation. We interpret our data in terms of previously described and modeled estimates for local, regional, and global climate changes during this time. Our study adds to a growing body of literature documenting the impacts of volcanism and ocean circulation on climate, especially leading up to the K-Pg extinction.

2. LOCALITY AND SAMPLE COLLECTION

Shell specimens were collected from three locations in the Liège-Maastricht region of northeastern Belgium and southeastern Netherlands: the Maastrichtian type section at ENCI quarry, the CBR Romontbos quarry, and the K-Pg boundary (KPB) section at the Geulhemmerberg subterranean galleries (GSGs) (Jagt and Jagt-Yazykova, 2012) (Fig. 1b). The ENCI quarry is located ~3.3 km south of the city of Maastricht in South Limburg, Netherlands (Fig. 1b). Maastrichtian-aged strata at this location include the Gulpen Formation (~67.1–78.9 Ma) overlain by the Maastricht Formation (~66.0–66.8 Ma) (Vellekoop et al., in prep.), the latter of which was sampled for this study of the uppermost Maastrichtian Stage. At this location, the stratigraphically highest exposure of the Maastricht Formation in the Meerssen Member predates the KPB by less than 100 kyr (Keutgen, 2018). The CBR Romontbos quarry is located ~4 km to the southwest of ENCI quarry, near Eben Emael, Liège, Belgium (Fig. 1b). The Maastricht Formation is also exposed at this outcrop, and samples were correlated to

align with the Maastricht Formation at ENCI quarry. In order to study the boundary interval itself, we also include a specimen from the nearby GSGs, which lie stratigraphically above the ENCI quarry and preserves the uppermost section of the Meerssen Member, including the K-Pg boundary interval. These subterranean galleries are located ~7 km east-northeast of ENCI quarry (Fig. 1b). There is an undetermined amount of missing time that is not exposed in either section (as indicated in Figure 2), which is constrained to less than 100 kyr.
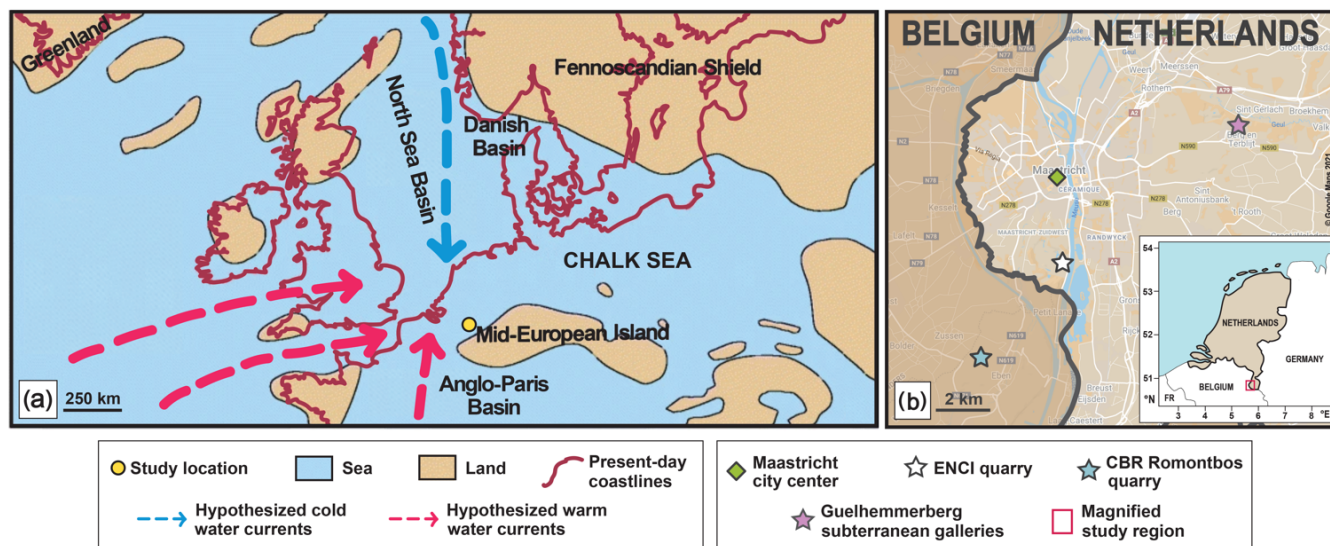

Figure 1: Paleogeography and sample localities for this study. (a) Late Cretaceous paleogeographic reconstruction of Europe and surrounding regions modified from Engelke et al. (2017) with the Maastricht region study location and hypothesized cold and warm water currents marked. (b) A modern-day map (from © Google Maps 2021) of the Maastricht region, located at the southernmost tip of the Netherlands (see inset), shows the relative position of the ENCI Quarry, Geulhemmerberg subterranean galleries, and CBR Romontbos quarry sampling localities to each other and to the city center of Maastricht.

At ENCI quarry, the Maastricht Formation consists predominantly of bioclastic calcarenites and calcirudites that coarsen upward, indicative of a gradual increase in hydrodynamic energy in the depositional environment (Schiøler, 1997; Vellekoop et al., in prep.). The lower part of the formation consists of fining-upward bioclastic silt and fine-grained sand, while the upper portion consists of fining-upward bioclastic sand beds (Schiøler, 1997; Vellekoop et al., in prep). Crossbedding and crosslamination are present in the lower parts of the Emaël, Nekum, and Meerssen Members (Zijlstra, 1994; Schiøler, 1997). This formation is interpreted to represent a shallow marine carbonate shelf that was subjected to fluctuating sea level and erosion (Schiøler, 1997). Prominent, fossiliferous horizons have been identified within the facies in this region (Felder, 1975; Zijlstra, 1988; Schiøler, 1997), including nine horizons in the Maastricht Formation at ENCI quarry (Fig. 2). Fossil shell specimens were collected from five of these horizons (Lichtenberg, ENCI, Romontbos, Lava, and Laumont), as well as from the top of the Emaël Member, the basal and middle intervals of the Nekum Member, and the basal interval of the Meerssen Member (Fig. 2).
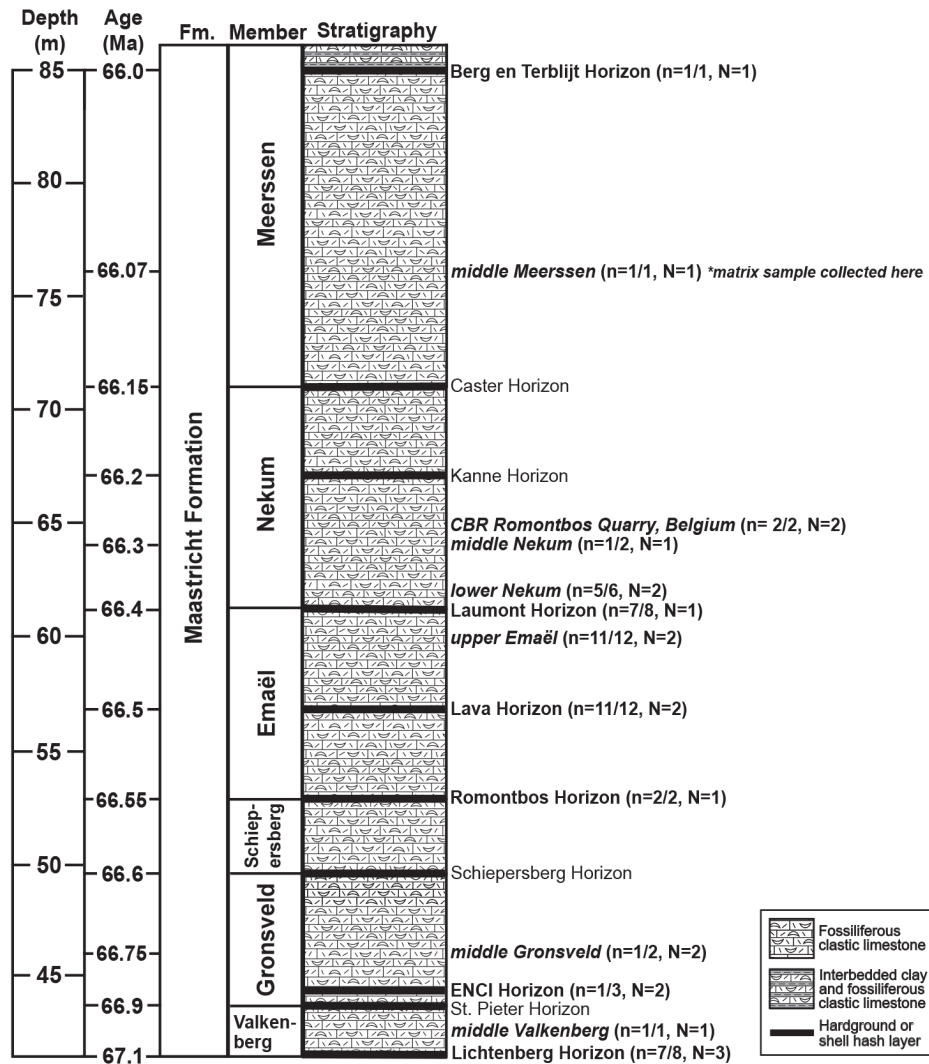
Figure 2: Composite stratigraphic section through the Maastricht Formation at ENCI quarry and Geulhemmerberg subterranean galleries. Number of specimens collected from horizons or intervals is listed on the right along with the number that passed diagenesis screening and the number of good specimens analyzed for clumped isotopes and interpreted here (n=passed/collected, N=clumped). Age model from Vellekoop et al. (in prep.). Berg en Terblijt Horizon assigned an age of 66.0 (Clyde et al., 2016; Sprain et al., 2018) and a depth of 85 m via correlation to ENCI quarry outcrop. Two specimens from the Nekum Member of the CBR Romontbos quarry in nearby Liège Province, Belgium were correlated to this section and are labeled therein.

In the GSGs, the uppermost Maastrichtian interval of the Meerssen Member is capped by the fossiliferous Berg en Terblijt Horizon, thought to mark the K-Pg extinction event and end of the Cretaceous Period (Smit and Brinkhuis, 1996). Directly above this horizon, interbedded layers of Danian-aged non-fossiliferous clay and fossiliferous limestone represent the KPB interval of the Maastricht Formation (Smit and Brinkhuis, 1996; Vellekoop et al., 2020) (Fig. 2). The specimen collected from the GSGs came from a shell hash layer directly above the Berg en Terblijt Horizon and below fossil-free clays. This fossil

assemblage is interpreted to be a tsunami deposit (Smit, 1999), and the specimen was likely alive right around the KPB and was deposited in this layer postmortem via the tsunami or other storm reworking. It was therefore assigned an age of 66.0 Ma (Clyde et al., 2016; Sprain et al., 2018).

Fossil shell specimens collected from the Maastricht Formation at the ENCI quarry, the CBR Romontbos quarry, and the GSGs included 60 bivalve specimens representing ten identified taxa of oysters, scallops, and clams (*Pseudoptera* sp*., Pycnodonte vesicularis, Acutostrea uncinella, Gryphaeostrea canaliculate, Agerostrea ungulata, Entolium membranaceum, Pinna* sp*., Neithea regularis, Ceratostreon* sp*.,* and *Rastellum* sp.), as well as four unidentified oysters and five unidentified bivalves. In these units, all biogenic aragonite has dissolved, leaving behind hollowed molds. All taxa sampled here originally formed calcite shells.

Taxa-specific clumped isotope vital effects in bivalves are considered uncommon, based on studies of modern bivalve taxa (Eagle et al., 2013; Henkes et al., 2013; Came et al., 2014). Therefore, well-preserved specimens are expected to faithfully record paleoenvironmental temperatures. Water depths for this location are estimated to be less than 20 m at all times, and often shallower (Hart et al., 2016), so reconstructed mean annual water temperatures are interpreted to approximate mean annual surface air temperatures. All measured specimens were sessile epifaunal suspension feeders and are assumed to have avoided significant lateral postmortem transport, apart from the specimen from the KPB tsunami horizon. Additionally, bulk matrix material from the Meerssen Member was analyzed for comparison to fossil shells, in order to assess the potential for diagenetic alteration of samples.

3. METHODS

3.1 Sample preparation

Carbonate samples were collected from the 60 fossil shell specimens by either hand-drilling or manual crushing in a mortar and pestle after removal of matrix material. One sample of matrix from the Meerssen Member was powdered and analyzed for comparison to co-occurring fossil shells. The sample powders were divided for trace element analysis and isotopic analysis. Fragments of some shell specimens were mounted for SEM observation to assess their preservation state.

3.2 Preservation assessment (SEM)

The isotopic composition of fossil shells is susceptible to post-depositional alteration via recrystallization, which can skew interpreted formation temperatures (Brand and Morrison 1987). All fossil shells collected for this study were screened for recrystallization using a combination of scanning electron microscopy (SEM) imaging and trace element detection methods. SEM imagery was performed on a JEOL JSM-7800FLV field-emission SEM in the Robert B. Mitchell Electron Microbeam Analysis Lab at the University of Michigan Ann Arbor. Of the 60 shell specimens, a subset of 17 specimens (with at least one

representing each analyzed horizon) were selected for SEM imagery of the shell microstructure and inspection for indications of dissolution and/or presence of secondary calcite growth.

3.3 Preservation assessment (trace elements)

Elevated levels of trace elements (Mn and Fe especially) in calcitic fossil material may indicate diagenesis/recrystallization of the calcite (Land, 1967; Möller and Kubanek, 1976; Brand and Morrison, 1987; de Winter et al., 2018). All 61 samples were analyzed in the Michigan Elemental Analysis Laboratory at the University of Michigan for Mn and Fe concentrations using a Thermo Scientific Quadrupole-ICP-MS (iCAP Q) equipped with an Elemental Scientific PrepFAST 2 Automation System. KED mode (He gas) was utilized for all isotopes. All samples were analyzed in 2% HNO_3 (w/v) (Optima grade), and sensitivity drift was corrected for with standard-sample bracketing methods.

3.4 Stable isotope analysis

Powders drilled or crushed from 60 shell specimens and one matrix sample were analyzed for oxygen ($\delta^{18}O$) and carbon ($\delta^{13}C$) stable isotope compositions. Of all the shells, 39 were analyzed using a Thermo-Finnigan Kiel IV automated carbonate device coupled to a MAT 253 gas source dual inlet mass spectrometer in the University of Michigan Stable Isotope Laboratory. Data were corrected for acid fractionation and normalized to the VPDB scale using NBS-18 and NBS-19 standards. Accuracy and precision were maintained at better than ±0.1 ‰ for both carbon and oxygen. The remaining 22 samples (21 shells, one matrix) were analyzed for $\delta^{18}O$ and $\delta^{13}C$ in conjunction with clumped isotope analysis in the University of Michigan Stable and Clumped Isotopes for Paleoclimatology and Paleoceanography (SCIPP) Laboratory (see below).

3.5 Clumped isotope analysis

Powders drilled or crushed from 15 shell specimens and one matrix sample were measured for clumped isotopic composition (Δ_{47}) in the University of Michigan SCIPP Lab between 2016–2020 using a Thermo-Finnigan MAT 253 dual inlet mass spectrometer and a manual sample preparation device described by Defliese et al. (2015), with updates to Porapak temperature as outlined by Petersen et al. (2016c). This measurement simultaneously acquires $\delta^{13}C$ and $\delta^{18}O$ of CO_2 gas and Δ_{47}, which is a function of temperature (Eiler, 2011). Raw voltages were converted to isotopic values using IUPAC/Brand parameters following Petersen et al. (2019). Raw Δ_{47} values were placed in the absolute reference frame of Dennis et al. (2011), using theoretical equilibrium values for heated (1000 °C) and water-equilibrated (25 °C) standard gases (0.0266 and 0.9198, respectively) and the 75 °C acid fractionation factor of +0.072 ‰ from Petersen et al. (2019). $\delta^{18}O$ of carbonate ($\delta^{18}O_{carb}$) was calculated from $\delta^{18}O$ of evolved CO_2 using an empirical acid fractionation factor defined using in-house carbonate standards independently calibrated to NBS-18 and NBS-19.

Powders from six more shells were analyzed in the SCIPP lab in 2021 using a Nu Perspective IRMS connected to a NuCarb device. This sample preparation device reacts samples in individual vials at 70 °C and follows an automated routine to clean and analyze CO_2. Raw Δ_{47} values were calculated from raw voltages using an R code modeled off the one in Petersen et al. (2019), adjusted to accommodate data formats from the Nu instrument. Isotopic values were converted into the absolute reference frame based on the measurements of four ETH standards with Δ_{47} values defined by the Intercarb project (Bernasconi et al., 2021). Data was corrected using an acid fractionation factor of +0.066 for 70 °C from Petersen et al. (2019).

Final, acid-corrected Δ_{47} values from both measurement periods were converted to temperature using the composite calibration of synthetic carbonates from Petersen et al. (2019) [$Temp = (0.0383*10^6)/(\Delta_{47}-0.258)-273.15$]. For better direct comparison with the previously published clumped isotope data from Meyer et al. (2018; 2019), the published data were reprocessed using IUPAC/Brand parameters, instead of the previously used Santrock/Gonfiantini parameters, and converted to temperature using the same procedure as our new data.

Seawater $\delta^{18}O$ ($\delta^{18}O_{sw}$) was calculated for these 21 shell specimens using measured $\delta^{18}O_{carb}$ and Δ_{47}-derived temperatures and the calcite-water relationship described by Kim and O'Neil (1997). All $\delta^{18}O_{sw}$ values are reported on the VSMOW scale.

3.6 Age model

Ages for all stratigraphic horizons, lithostratigraphic boundaries, and specimens were determined by updating the Keutgen (2018) age model using known biostratigraphic markers and bulk carbon isotope data (Vellekoop et al., in prep.). All ages have an uncertainty of ± 0.05 Ma, with the exception of the Lichtenberg Horizon (uncertainty of ± 0.2 Ma) and the Berg en Terblijt Horizon (uncertainty of ± 0.01 Ma).

4. RESULTS

4.1 Preservation and sample screening

Isotopic compositions may be affected by dissolution, recrystallization/replacement of shell material in a diagenetic environment, or overgrowth of secondary material. Clumped isotopic compositions may additionally be affected by solid-state bond reordering, which reduces heavy isotope pair bonding in the crystal lattice and overprints the original recorded temperature without any mass transfer. Bond reordering can occur if samples are heated above 100–150 °C (Henkes et al., 2014; Winkelstern and Lohmann, 2016), such as during burial. This process is invisible to our direct screening methods (e.g., SEM, trace elements) but can be constrained from estimates of maximum burial depth/temperature.

Regional geologic evidence suggests a relatively shallow burial history for these strata. In the southern Netherlands, the Roer Valley Graben contains several basin-wide unconformities dated to the Late Cretaceous and middle Paleocene that signify two basin inversions, leaving the Maastrichtian and Danian strata relatively undisturbed (Luijendijk et al., 2011 and

references therein). Outstandingly well-preserved mosasaur skeletons and hollow aragonitic molds in the Maastricht Formation further indicate a lack of burial or significant diagenetic fluid flow during this time (Dortangs et al., 2002; Jagt et al., 2016). Overall, these burial conditions are not expected to result in bond reordering in any samples.
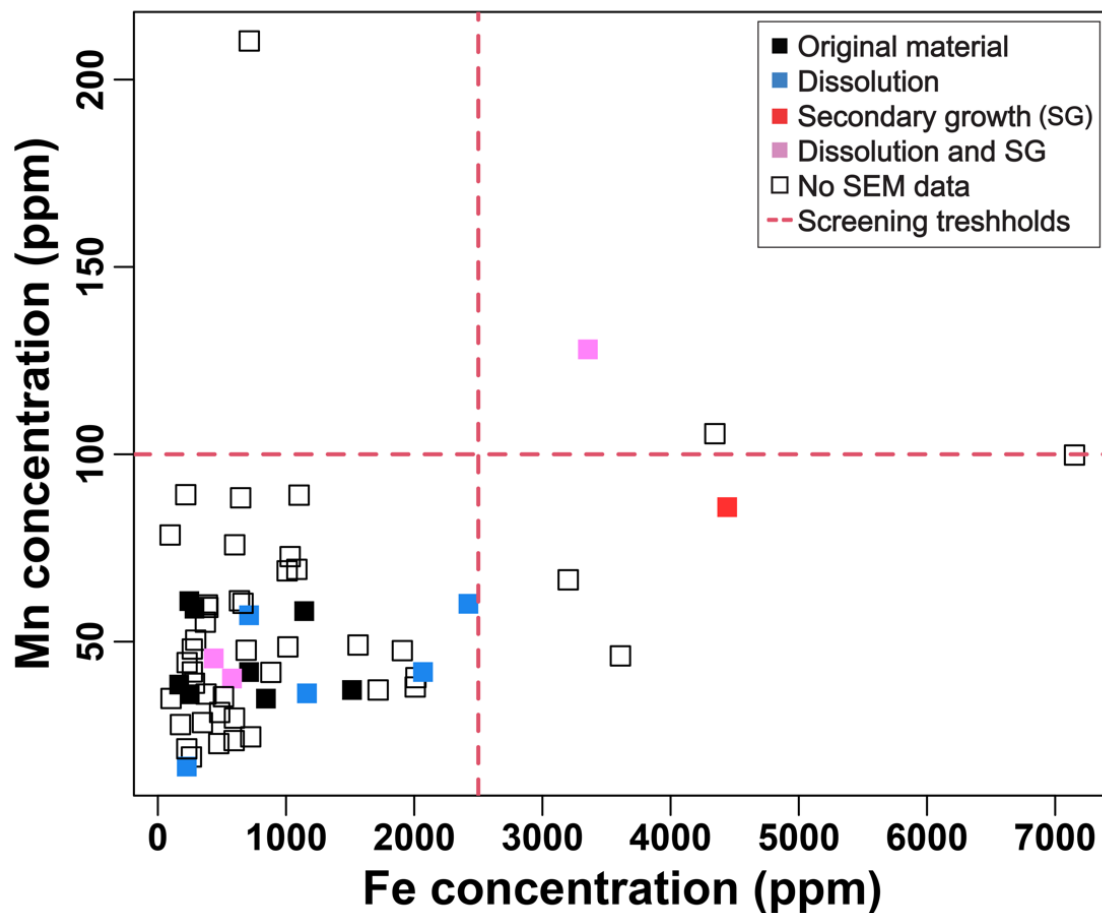
Figure 3: Iron and manganese concentrations of all samples, used for diagenesis screening. Dashed red lines represents screening thresholds of 2500 ppm for Fe and 100 ppm for Mn, selected to screen out most samples showing secondary growth while keeping most samples showing good preservation under SEM. This screening resulted in seven samples being excluded for elevated trace elements and two more for evidence of secondary growth under SEM (see text).

Evidence of dissolution of original shell material and/or overgrowth of secondary, diagenetic calcite are observable in SEM textures and/or trace element concentrations. In the 60 shell specimens tested for trace elements, Mn ranges from 17–210 ppm, and Fe ranges from 96–7151 ppm. The matrix sample exhibits 60 ppm Mn and 664 ppm Fe. By aligning the SEM observations with the trace element results, threshold values of 100 ppm and 2500 ppm were selected for Mn and Fe, respectively. These thresholds screen out all but two shell samples that showed secondary growth under SEM, while keeping

all samples that exhibited original material (Fig. 3). These thresholds are more conservative than those proposed by other studies (Morrison and Brand, 1987; Voigt et al., 2003; Ullmann et al., 2013, de Winter et al., 2018), but, in total, still only result in the removal of nine specimens out of 60, which are not included in discussions of isotopic compositions below. Isotopic evidence supports that these are conservative trace element thresholds. Despite being excluded based on SEM and trace element results, the isotopic values of excluded samples were not substantially different than other shells that passed diagenesis screening (none of the excluded samples show significantly different $\delta^{18}O_{carb}$ values, only two exhibit lower-than-normal $\delta^{13}C_{carb}$, and one has a higher-than-normal Δ_{47}-derived temperature; Figs. S1, S2, S3). Additionally, the one sample of matrix material (taken from the Meerssen Member) showed a temperature of ~20 °C, indicating that the bulk matrix—which is more likely to be affected by recrystallization or reordering than a dense calcite shell—has also not undergone isotopic alteration (Fig. A3).

4.2 Stable isotopes

Of the 60 shell specimens measured for $\delta^{18}O_{carb}$ and $\delta^{13}C_{carb}$, nine were excluded from further interpretation due to evidence for diagenesis (described above). The remaining 51 specimens exhibit a range of $\delta^{18}O_{carb}$ values between -2.5 ‰ and -0.5 ‰ VPDB with the exception of two outliers that measured +0.4 ± 0.1 ‰ VPDB and +0.7 ± 0.1 ‰ VPDB (Fig. A1). Excluding these outliers, the average $\delta^{18}O_{carb}$ value throughout the section is -1.3 ± 0.4 ‰ VPDB. Although divergent samples in $\delta^{18}O_{carb}$ do not show divergent $\delta^{13}C_{carb}$ values, we nevertheless excluded them from further calculated averages. The resultant mean $\delta^{13}C_{carb}$ is 2.8 ± 0.6 ‰ VPDB with all values ranging between 1.4 ‰ and 4.0 ‰ VPDB (Fig. A2). The taxa *Neithea regularis*, *Rastellum* sp., and *Ceratostreon* sp. exhibit notably lower $\delta^{13}C$ values (1.1–2.1 ‰) relative to other species, potentially indicating higher incorporation of metabolic carbon, but $\delta^{18}O_{carb}$ values remain similar to other taxa. No other taxa show distinguishable offsets from the mean $\delta^{18}O_{carb}$ or $\delta^{13}C_{carb}$ values (Figs. A1, A2). Nevertheless, the number of specimens representing most of the taxa is too small to make reliable conclusions.

Bulk carbonate $\delta^{18}O$ analysis of the Maastricht Formation at ENCI quarry reveals an increasing then stabilizing trend from the bottom of the formation toward the top (Vellekoop et al., in prep.) (Fig. A1). The lowest bulk carbonate $\delta^{18}O$ values (less than -1.6 ‰ VPDB) occur in the Valkenberg Member where bulk carbonate values align with bivalve $\delta^{18}O_{carb}$ values (Fig. A1). Above the Valkenberg Member, bulk matrix $\delta^{18}O_{carb}$ increases steadily through the Gronsveld and Schiepersberg Members before leveling off between -0.55 ‰ and -0.03 ‰ VPDB throughout the Emaël and Nekum Members (Fig. A1). Over this interval, bivalve $\delta^{18}O_{carb}$ values are generally lower than the bulk carbonate, with values ranging between -1.6 ‰ and -0.5 ‰ VPDB in the Emaël and Nekum Members (Fig. A1). This relationship holds true in the Meerssen member, where the matrix sample measured as part of this study is elevated above bivalve $\delta^{18}O_{carb}$ by ~1 ‰ and continues the constant trend in bulk carbonate $\delta^{18}O_{carb}$ from the Emaël and Nekum Members, plotting at -0.3 ‰ VPDB (Fig. A1).

4.3 Temperature estimates

Four of the 21 shell specimens measured for Δ_{47} were excluded from further interpretation as part of the group of nine samples displaying evidence of diagenesis (described above) (Fig. A3). The 17 samples that pass diagenetic screening criteria exhibit paleotemperatures ranging from 11.7–25.1 °C with a mean value of 19.2 ± 3.8 °C (Fig. 4). In the four instances where multiple taxa were sampled from the same horizon, there is generally strong agreement between reconstructed temperatures (all but one have means within 1 °C, well within error). A fluctuating temporal trend is observed in which paleotemperatures peak at 66.37 Ma, followed by a decrease by 66.1 Ma. The sample from the shell hash layer representing the KPB in the GSGs indicates a second warming from 66.1 to the boundary at 66.0 Ma of ~9 °C, though this trend relies on only two datapoints (Fig. 4). The initial warming coincides with the named "Late Maastrichtian Warm Event" (Woelders et al., 2018, Hull et al., 2020) and the onset of Deccan volcanism 66.413 ± 0.067 Ma (Sprain et al., 2019), within the error of our age model.
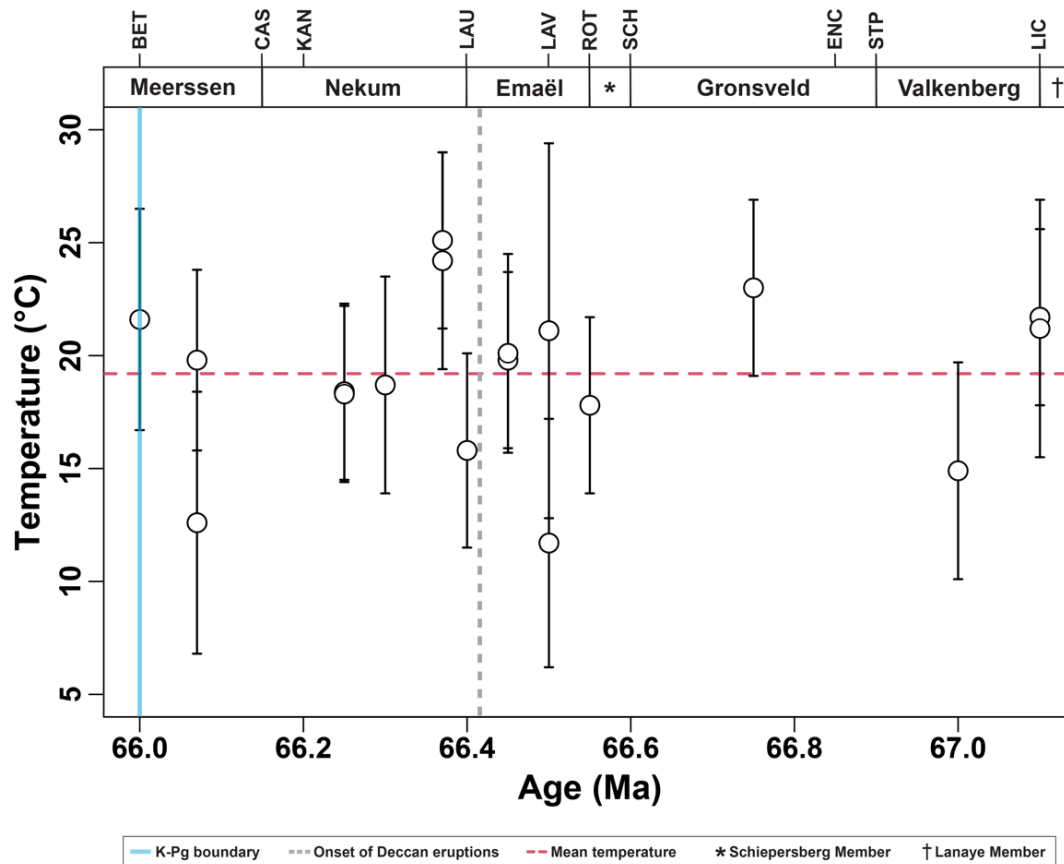
Figure 4: Maastrichtian paleotemperatures derived from Δ_{47}. Both internal and external standard error were calculated for all data points, and the larger of the two errors for each point is depicted here as an error bar. Samples that did not pass SEM and trace element diagenesis screening are not included on this plot. Onset of the main Deccan Traps eruptions (grey dotted line) at 66.413 Ma (Sprain et al., 2019). K-Pg boundary (blue line) at 66.0 Ma. Mean temperature of 19.2 °C (red dashed line). Member names and horizon abbreviations are labeled across top of figure.

4.4 Seawater δ¹⁸O estimates

Calculated $\delta^{18}O_{sw}$ values ranged from -1.8 to 1.2 ‰ VSMOW (Fig. 5). The average $\delta^{18}O_{sw}$ value is -0.2 ± 0.9 ‰ VSMOW, above but within error of the ice-free mean ocean water estimate of -1.0 ‰ VSMOW. This heavier average $\delta^{18}O_{sw}$ value is consistent with the presence of some continental ice volume (presumed to be located on the Antarctic continent) during the "cool greenhouse" Maastrichtian interval (Miller et al., 2005; Petersen et al., 2016a, Ladant and Donnadieu, 2016). There are generally no significant offsets in $\delta^{18}O_{sw}$ between taxa when multiple taxa were sampled within a given horizon. These data show a similar temporal trend to that of the paleotemperature data (Fig. 5). The similarity in trajectories between temperature and $\delta^{18}O_{sw}$ is required because temperature shows no correlation with $\delta^{18}O_{carb}$ (Fig. 5).
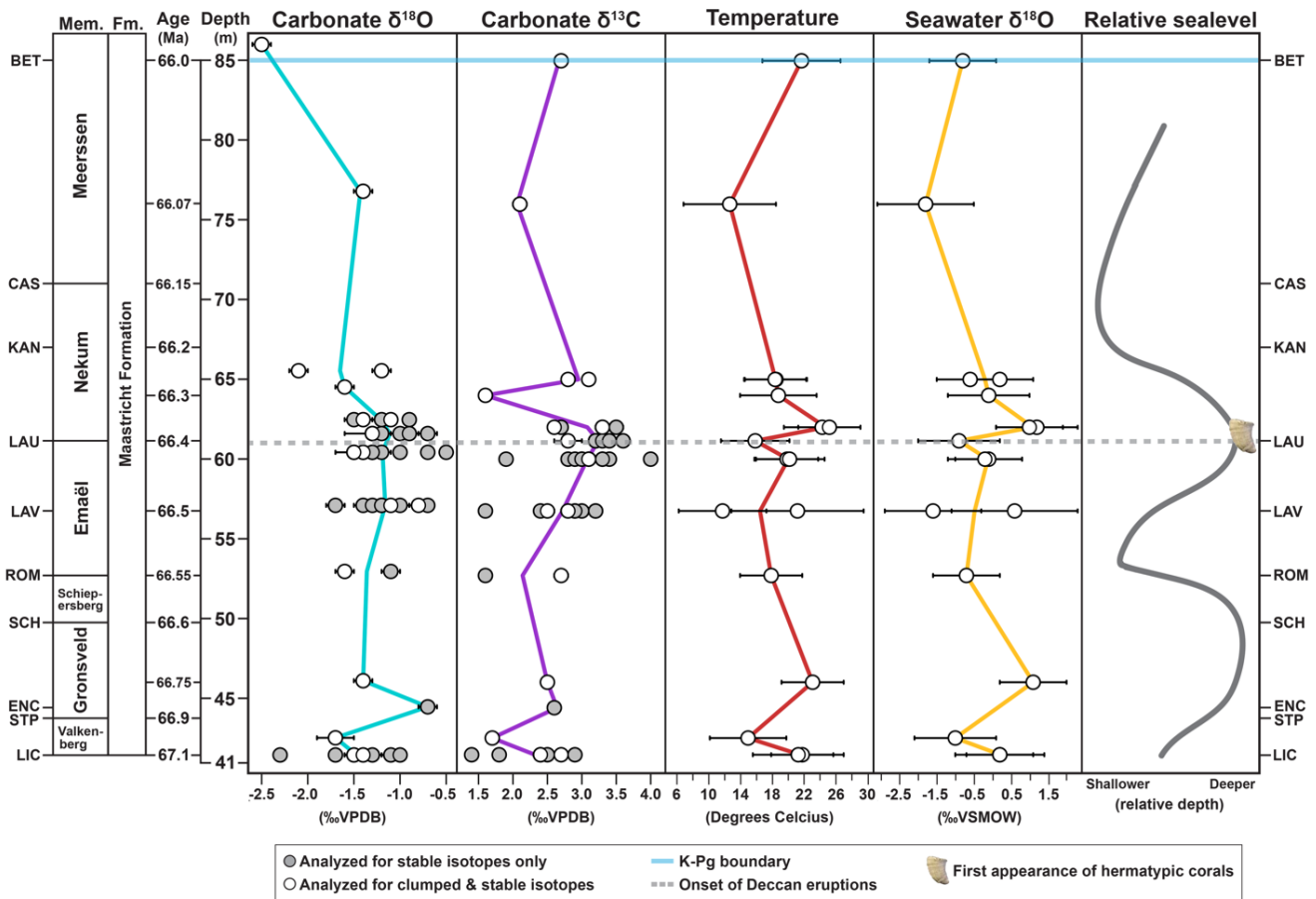
Figure 5: Isotopic composition and paleotemperature measurements compared to inferred relative sea level in the Maastricht Formation. For horizons with more than one data point for one parameter, the average of all points in that horizon is intersected by the trendline. If no error bars are visible, the uncertainty is smaller than the size of the symbol. Age model from Vellekoop et al. (in prep.). The relative sea level curve is based on that derived by Schiøler et al. (1997) and fitted to the depth/age model used in this study. Hermatypic coral appearance data is from Leloux (1999). Onset of the main Deccan Traps eruptions (grey dotted line) at 66.413 Ma (Sprain et al., 2019). K-Pg boundary (blue line) at 66.0 Ma.

We observe peak $\delta^{18}O_{sw}$ values in the middle of the Gronsveld Member (1.1 ± 0.9 ‰ VSMOW; depth of ~46 m) and at the base of the Nekum Member (1.2 ± 1.1 ‰ VSMOW; depth of ~62 m) (Fig. 5). The lowest $\delta^{18}O_{sw}$ values occur at the Lava Horizon in the Emaël Member (one sample at -1.6 ± 1.3 ‰ VSMOW; depth of 56.75 m) and in the middle part of the Meerssen Member (-1.8 ± 1.3 ‰ VSMOW; depth of ~76 m) (Fig. 5). The $\delta^{18}O_{sw}$ values appear to fluctuate in time with similar variations in temperature and $\delta^{13}C_{carb}$ (Fig. 5).

4.5 Revised temperature estimates from previously published clumped isotope data

Reprocessing of published Maastrichtian clumped isotope data from Meyer et al. (2018; 2019) resulted in substantially higher (~6 °C) average temperatures for four locations and slightly lower (>1 °C) average temperatures for the remaining four sites (Table 1). Our reprocessed Meyer et al. (2018; 2019) temperatures align more closely with previously published data and modeling studies (Fig. 6). Notably, an originally anomalously low paleotemperature of 6.7 °C for a sample from the Navesink Formation in Monmouth County, New Jersey (paleolatitude of 37° N; Meyer et al., 2018) increased to 13.8 °C after reprocessing (Table 1).

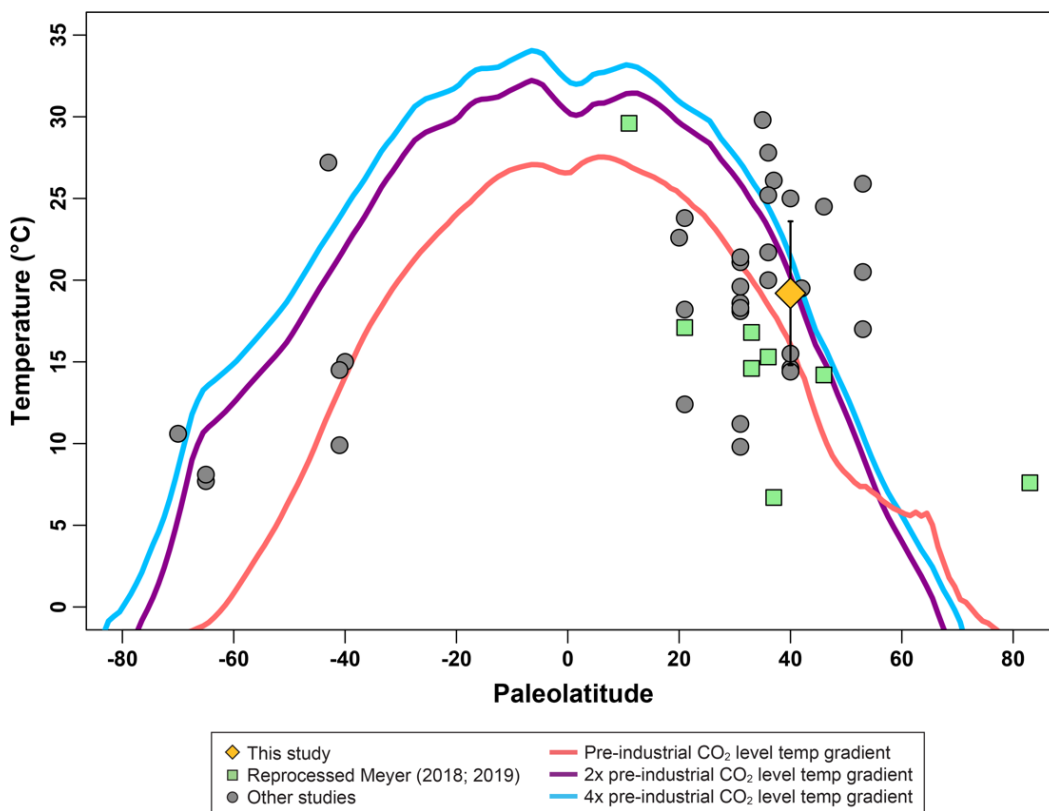**Figure 6: Average late Maastrichtian temperatures from numerous clumped isotope studies at different paleolatitudes around the globe.** New data from this study and reprocessed data from Meyer et al. (2018; 2019) are included. The three lines are global climate models created with Late Cretaceous conditions and varying pCO$_2$ levels (Tabor et al., 2016). All studies used in this figure are listed in Table A1.

13

Table 1: Clumped isotope-derived temperatures from Meyer et al. (2018; 2019) reprocessed using the same procedure as our data. Data from this study is included and highlighted in red. Paleolatitudes determined via www.paleolatitude.org (van Hinsbergen et al., 2015), apart from the Moreno Formation study by Meyer et al. (2019) for which paleolatitude was estimated by Kodama and Ward (2001) due to the location being on an unconstrained plate.

Study	Sample type	Formation and locality	Paleolat. (°N)	Approx. age (Ma)	Original avg. temp. (°C)	Reprocessed avg. temp. (°C)
Meyer et al. (2018)	Oysters	Navesink Formation Monmouth County, NJ, USA	37	70.7	6.7	13.8
Meyer et al. (2018)	Oysters, clams, gastropod	Ripley Formation Western Tennessee, USA	36	73.5	15.3	21.5
Meyer et al. (2018)	Oysters, clams	Clayton, Prairie Bluff, Ripley Fms. Moscow Landing, AL, USA	33	65.0–74.0	16.8	22.1
Meyer et al. (2018)	Oysters, clams, belemnite	Pee Dee Formation Burches Ferry, SC, USA	33	71.4	14.6	20.6
Meyer et al. (2019)	Clam, bivalve	Prince Creek Formation North Slope, AK, USA	83	69.4	7.6	7.4
Meyer et al. (2019)	Belemnites, bivalve	Unidentified formation Scania, Sweden	46	69.2–72.3	14.2	13.9
Meyer et al. (2019)	Oysters, clams	Moreno Formation Merced County, CA, USA	21	69.7–78.0	17.1	16.5
Meyer et al. (2019)	Oysters	Unknown formation Fezzan region, Libya	11	70.9–71.4	29.6	29.2
This study	Oysters, clams, scallops	Maastricht Formation SE Netherlands & NE Belgium	40	66.0–66.8	NA	19.2

5. DISCUSSION

5.1 Local to global Maastrichtian climate

New data presented here indicates mean annual ocean temperatures in the Maastricht region (paleolatitude ~40° N; van Hinsbergen et al., 2015) varied from 11.7–25.1 °C between 67.1–66.0 Ma, with a mean temperature of 19.2 ± 3.8 °C. This is much warmer than the modern-day climate of Maastricht but agrees closely with the mean of other published Maastrichtian marine paleotemperatures from sites located between 30–50° N (mean of 19.8 ± 5.2 °C; n = 23 studies; Table A1). For comparison, modern-day Maastricht has an average annual air temperature of 9.8 °C (Maastricht Climate, 2021). New paleotemperature estimates also align with evidence from Maastrichtian-aged fossil plants which suggest that on-land temperatures at 40° N were around 15 °C (Golovneva, 2000) and that near 49° N, air temperatures varied from 10–18 °C during this time interval (Wilf et al., 2003). Our mean temperature also agrees well with zonal mean temperatures generated by general circulation models using Late Cretaceous paleogeography and atmospheric pCO_2 levels of either two- or four-times pre-industrial levels (Tabor et al., 2016; Ladant et al., 2020) (Fig. 6).

5.2 Ocean circulation, sea level, and/or precipitation changes

Paleogeographic reconstructions (Engelke et al., 2017; Scotese, 2021) (Fig. 1a) and presence of seagrass fossils (Hart et al., 2016; van der Ham et al., 2017) indicate that during the Campanian-Maastrichtian, the study site was located on a large, shallowly submerged carbonate platform. Over the Late Cretaceous, eustatic sea level fluctuated multiple times, including one sea level transgression (KMa5) in the latest Maastrichtian at 66.8 Ma (Haq, 2014). Sea level based on the relative abundance of the palynomorph *Paralecaniella* in ENCI quarry sediments—the same section as our fossils—indicate Maastrichtian fluctuations that differ from the global eustatic curve (Schiøler et al., 1997) (Fig. 5). Since high relative abundances of this acritarch taxon are suggested to reflect marginal-marine to restricted-marine conditions under high hydrodynamic conditions (Brinkhuis and Schiøler 1996; Schiøler et al., 1997), observed fluctuations are interpreted as local sea level changes. Nevertheless, seagrass and foraminifera indicate that water depths remained less than 20 m at all times, and often shallower (Hart et al., 2016).

Although this local sea level record derived from palynological abundances may have some issues at a fine scale related to minimal consideration of sedimentology and geochemistry (Vellekoop et al., in prep.), we see a notable correlation between it and many of our isotopic parameters. Peak $\delta^{18}O_{sw}$ values, high temperatures, and higher $\delta^{13}C_{carb}$ values correlate to periods of maximum sea level, while lower $\delta^{18}O_{sw}$ values, cooler temperatures, and lower $\delta^{13}C_{carb}$ values correspond to periods of relatively lower sea level (Fig. 5). Alternatively, environmental factors other than sea level might have driven the observed high abundances of *Paralecaniella* in the type-Maastrichtian, such as biological responses to local changes in hydrodynamic conditions and salinity, which would also be reflected in the $\delta^{18}O_{sw}$ record presented here.

We propose that the observed correlation between environmental conditions and reconstructed local sea level is the result of fluctuating ocean circulation patterns. Paleogeographic reconstructions suggest the presence of a seaway connecting the Arctic Ocean to this study site during the Late Maastrichtian (Engelke et al., 2017; Scotese, 2021) (Fig. 1a). Modeling studies show that increased isolation of the Arctic made it fresher during the Maastrichtian (Ladant et al., 2020), suggesting that this boreal water mass was both cooler in temperature and depleted in $\delta^{18}O$. As a result, the Maastrichtian type region would have been under the influence of relatively cool, depleted water masses. Our study site was situated on a shallow carbonate platform surrounded by small landmasses, the exact size and position of which are difficult to define (Engelke et al., 2017; Scotese, 2021) (Fig. 1a). During periods of low relative sea level, the land masses of the Rhenohercynian Zone (Rhenish Massif, London-Brabant Massif) would have blocked southern currents originating in warmer regions, which would likely be saltier and have higher $\delta^{18}O_{sw}$ values due to evaporative enrichment. However, as large parts of these land masses were relatively flat and low-lying during the Upper Cretaceous (Vandenberghe et al., 2014), relatively minor increases in sea level could potentially breach sills or island barriers, changing both the position of ocean currents and the dominant water mass in a given area. Indeed, lithostratigraphic studies in the region have shown that during various phases in the Campanian-Maastrichtian, the structural highs of the nearby London-Brabant Massif were fully submerged (e.g., Dusar and Lagrou, 2007). As a result,

during sea level lows, the Maastrichtian type region would have been predominantly under the influence of colder, depleted water masses, while during sea level highs, the influence of warmer, more enriched water masses likely increased.

Similar interactions between cooler and warmer water masses have been called upon to explain unexpected distributions in warm-water ammonite fauna in the Coniacian-Santonian of Europe (Remin et al., 2016) and remarkably southerly occurrences of cold-water belemnites in Late Cenomanian France (Gale and Christensen, 1996). In this case, the authors suggest that warm waters flowing east to west from the proto-Tethys competed with cooler waters flowing southward between Greenland and Scandinavia (see their Figure 10). We suggest a similar mechanism applied to Late Maastrichtian paleogeography and water masses (Fig. 1a). Ostracod assemblage changes indicate increasing contribution of warm Mediterranean/Tethyan waters in the latest Maastrichtian (Bless, 1988). Faunal abundance differences along the US East Coast indicate the presence of an ancient Gulf Stream-like current as far back in time as the Maastrichtian (Watkins and Self-Trail, 2005), which would have warmed the Maastricht region above its expected temperature for latitude when bathed in water from the south, as the modern-day Gulf Stream does for western Europe. In summary, the cooler water mass may have originated in the Arctic, whereas the warmer water mass may have come from the southwest (Fig. 1a).

Fluctuations in $\delta^{13}C$ appear to correlate with changes in temperature and $\delta^{18}O_{sw}$ (Fig. 5). In this hypothetical model of alternating influence of southern and northern source waters, this could indicate different $\delta^{13}C$ of dissolved inorganic carbon ($\delta^{13}C_{DIC}$) in the two water masses. The exact values of $\delta^{13}C_{DIC}$ in either water mass are difficult to define because of overprinting by $\delta^{13}C$ vital effects in some taxa (*Neithia* sp.*, Rastellum* sp.). Looking at the most common taxa (*Acutostrea*), variations on the order of 0.5‰ VPDB—or possibly as much as 1 ‰—are possible between horizons. This is similar to variability seen in the modern Atlantic Ocean (Eide et al., 2017) and is therefore plausibly driven by alternating water masses of differing $\delta^{13}C_{DIC}$. In this scenario, the colder, northern (Arctic) water mass would be more depleted in $\delta^{13}C_{DIC}$ than the southern source water.

This dataset is not capable of distinguishing between the above, preferred hypothesis and a temporally variable input of isotopically depleted freshwater. During times of lower sea level, partial basin restriction may have occurred, allowing local freshwater inputs to lower $\delta^{18}O_{sw}$ values. In maritime regions such as modern Bermuda, despite lack of elevation or substantial landmass, precipitation is depleted in $\delta^{18}O$ by 4–5 ‰ VSMOW relative to seawater (Zhang et al., 2021). Additionally, surface runoff may contain dissolved terrestrial organic matter depleted in $\delta^{13}C$, which could explain the correlation between $\delta^{18}O_{sw}$ and $\delta^{13}C$ through our study period. However, it is difficult to explain how local freshwater in a subtropical environment surrounded by low-lying landmasses could be substantially colder than local seawater, so we favor the variable water mass hypothesis over a local freshwater contribution.

Yet another possible interpretation of the co-variation between fluctuating temperature and $\delta^{18}O_{sw}$ trends is via climate-related reorganization of atmospheric circulation, moving broad precipitation bands north and south over the study region. An enhanced hydrological cycle has been hypothesized for the latest Cretaceous (e.g., Woelders et al., 2017) due to increased

zonal surface winds and ~20 % stronger Hadley circulation in the Northern Hemisphere (Bush and Philander, 1997). If, during warmer climates, precipitation bands moved such that the Maastrichtian type region experienced less rainfall, $\delta^{18}O$ enrichment of surface waters would coincide with warmer temperatures and vice versa. This is difficult to assess, even in global climate model simulations, as model proficiency in reconstructing paleo-precipitation regimes is difficult to validate/calibrate. The rough correlation with $\delta^{13}C$ is also difficult to explain in this scenario.

5.3 Temperature trends and a record of Deccan-induced warming

Multiple paleoclimate records document a late Maastrichtian warming event (LMWE) (e.g., Stott and Kennett, 1990; Li and Keller, 1998; Petersen et al., 2016a; Woelders et al., 2017; Woelders et al., 2018; Barnet et al., 2019; Gao et al., 2021; Nava et al., 2021), beginning gradually at 66.4 Ma with more rapid warming at 66.3 Ma (Hull et al., 2020). This timing of the LMWE aligns it with the onset of LIP volcanism in the Indian subcontinent, based on ^{40}Ar-^{39}Ar ages for the oldest basalts of the Deccan Traps (66.413 ± 0.067 Ma; Sprain et al., 2019) and shifts in marine osmium isotope ratios towards mantle values beginning ~400 kyr prior to the KPB (Ravizza and Peucker-Ehrenbrink, 2003; Hull et al., 2020).

The Δ_{47}-derived temperature record generated here documents a warming in the Nekum Member from 66.4 Ma (15.8 ± 4.3 °C) to 66.37 Ma (24.7 ± 4.8 °C) (Fig. 4). The magnitude of this warming is calculated as 8.9 °C going from adjacent horizons or, more conservatively, 7.0 °C comparing the warmest horizon to a pre-event baseline averaging the preceding six points (17.7 ± 3.5 °C). Considering the size and meaning of the 1SE error bars and the small number of samples representing peak warmth (n=2; Fig. 4), this warming event is only barely distinguishable as differing from the mean of the full record. However, a number of other lines of evidence support the interpretation of this warming as an expression of the LMWE.

Based on a newly updated age model (Vellekoop et al., in prep), the warmest Δ_{47}-derived temperatures align with the onset of earliest Deccan eruptions and the age of the globally defined LMWE (Fig. 4). The dinocyst *Palynodinium grallator*—a marker for the LMWE at northern mid-latitudes (Vellekoop et al., 2018; 2019)—first appears in the Maastricht Formation in the Nekum Member (Schioler et al., 1997; Vellekoop et al., 2019). Thermophilic hermatypic scleratinian macrofossils also first emerge in high abundances in the Nekum Member (Liebau, 1978; Leloux, 1999). Together, these records suggest that the LMWE is preserved in the Nekum Member at ENCI quarry and that the warmer Δ_{47}-derived temperatures found there are likely real.

We observe a second warming directly preceding the boundary (~66.1 Ma) in our record (Fig. 4), which is also visible in other records (e.g., Wilf et al., 2003; Petersen et al., 2016a, Woelders et al., 2017; Zhang et al., 2018). The magnitude of this second warming is uncertain given the low density of samples immediately prior from which to determine a baseline pre-excursion temperature, and suffers from the same statistical issues as defining the LMWE (limited samples, large 1SE error bars). Therefore, we opt not to overinterpret this. A higher sample density through this section could potentially resolve some of this uncertainty.

6. CONCLUSIONS

This study presents a new clumped isotope-based paleotemperature time series from the latest Cretaceous in northwestern Europe. The Δ_{47} analyses from the Maastrichtian type section and surrounding outcrops reveal a mean temperature of 19.2 ± 3.8 °C and an average $\delta^{18}O_{sw}$ of -0.2 ± 0.9 ‰ VSMOW, consistent with a subtropical shallow marine environment. This average temperature aligns well with other paleothermometry studies from similar paleolatitudes and with modeled Maastrichtian paleotemperatures. Increasing Δ_{47}-based temperatures at ~66.4 Ma, in conjunction with other indicators, are interpreted to reflect a regional manifestation of the global LMWE and directly link pre-KPB warming in northwest Europe to CO_2 emissions from Deccan Traps volcanism.

Covariations in temperature, $\delta^{18}O_{sw}$, and (to a lesser degree) $\delta^{13}C$ from horizon to horizon may reflect the varying influences of different water mass at different times. We hypothesize that colder waters with lower $\delta^{18}O_{sw}$ and $\delta^{13}C_{DIC}$ may have originated from the Arctic and reached the study site via a passageway between Greenland and Scandinavia (Fig. 1a). Warmer waters with higher $\delta^{18}O_{sw}$ and $\delta^{13}C_{DIC}$ may have been sourced from a proto-Tethys to the southeast or proto-Atlantic to the southwest (Fig. 1a). Alternating influence of these two proposed water masses may be linked to regionally fluctuating sea level and the presence of more submerged or more exposed bathymetric highs allowing or preventing southern water flowing north.

Overall, the fossils of the Maastricht Formation are effective paleotemperature archives that reveal linkages between local sea level changes, Deccan Traps volcanism, and ocean temperature on the European continent in the lead-up to the end-Cretaceous.

Additional plots and tables to supplement the manuscript.
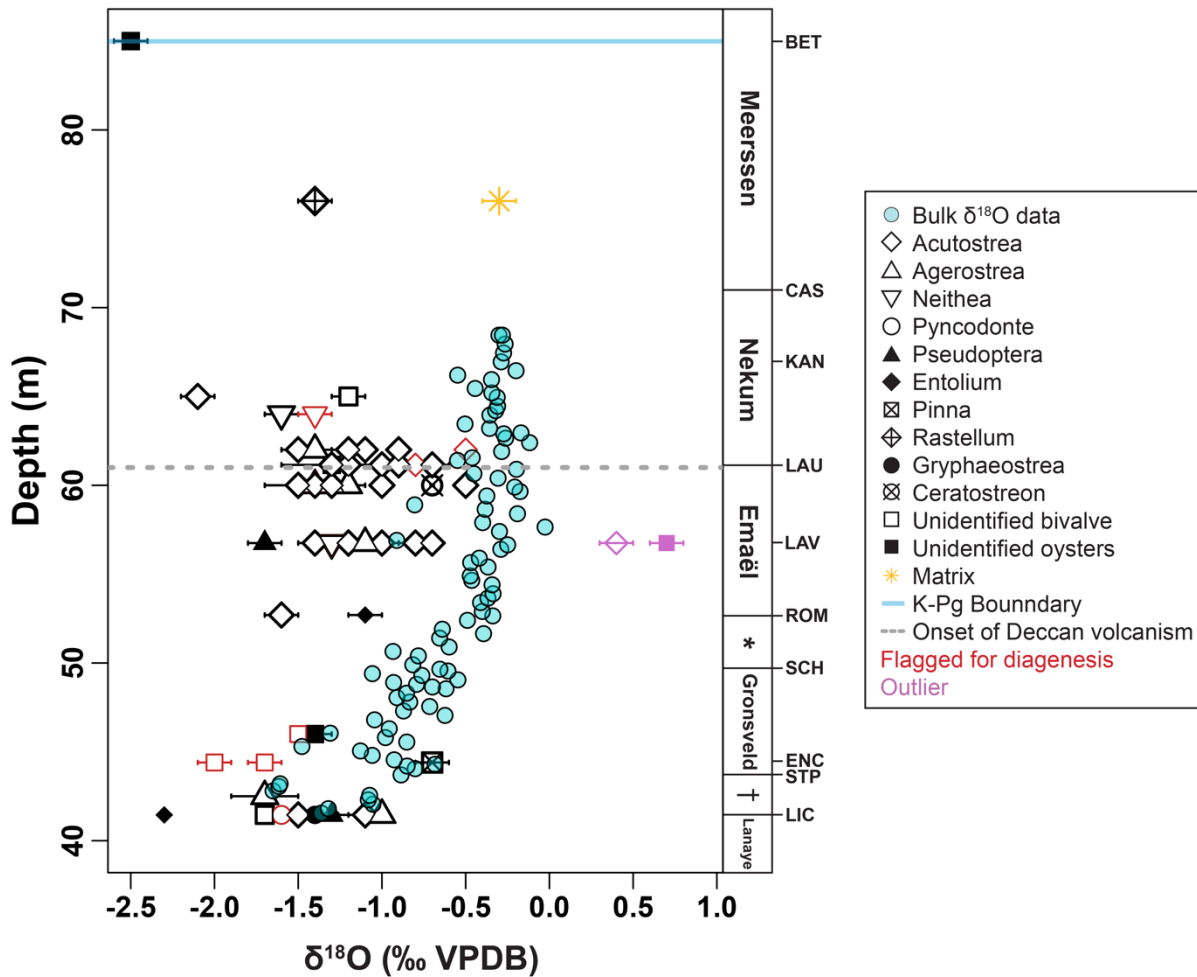
Figure A1: Oxygen isotope values of shell specimens and bulk carbonate. Bulk carbonate $\delta^{18}O$ data from ENCI quarry are from Vellekoop et al. (in prep.). Red data points (flagged for diagenesis by trace element and/or SEM analysis) and purple points (outliers) were excluded from interpretation. If no error bars are visible, the uncertainty is smaller than the size of the symbol. Onset of the main Deccan Traps eruptions (grey dotted line) at 66.413 Ma (Sprain et al., 2019). K-Pg boundary (blue line) at 66.0 Ma. Member names and horizon abbreviations are labeled along right side of figure. Laneye Member is part of underlying Gulpen Formation. *Schiepersberg Member; †Valkenberg Member.
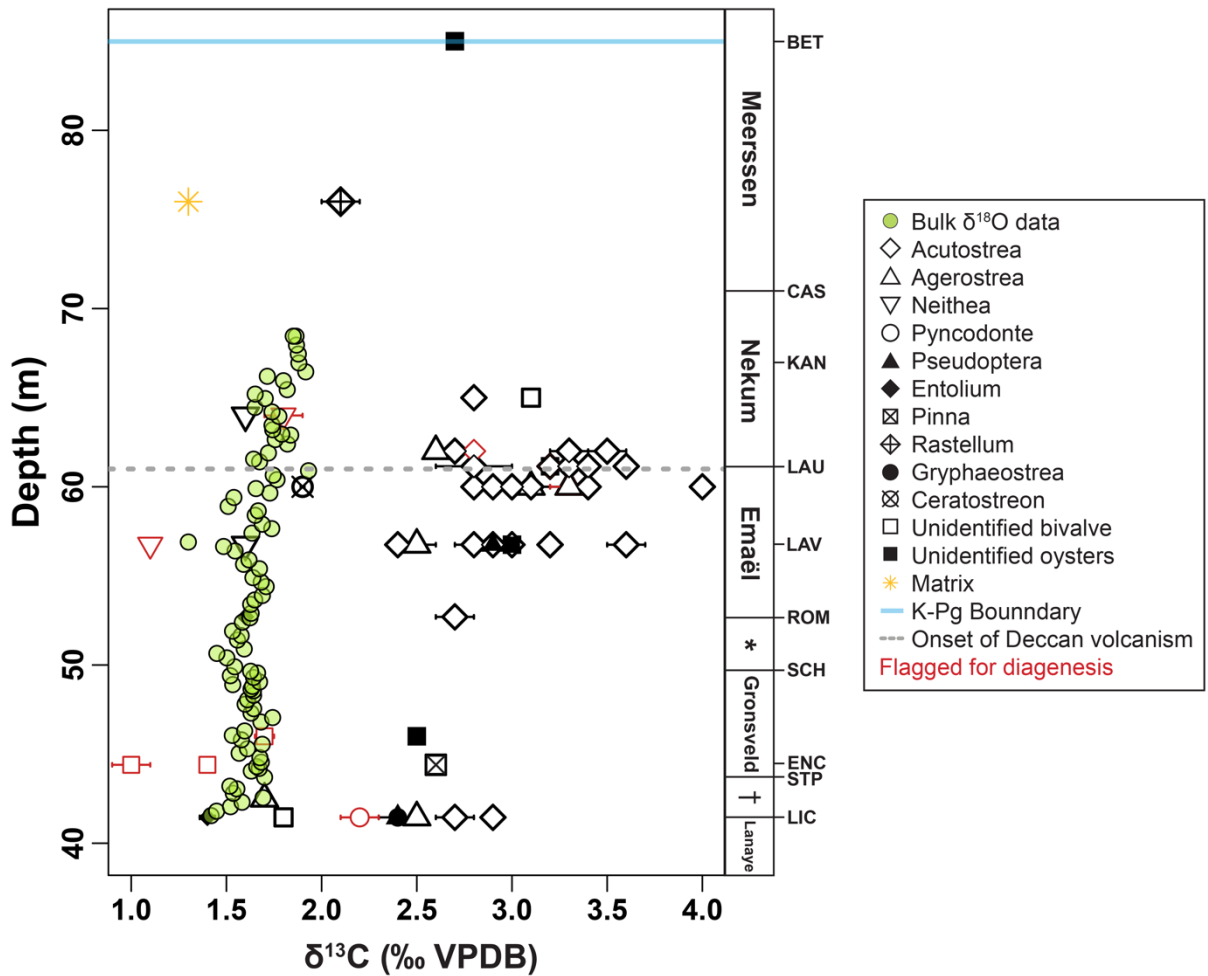
Figure A2: Carbon isotope values of shell specimens and bulk carbonate. Bulk carbonate $\delta^{13}C$ data from ENCI quarry are from Vellekoop et al. (in prep.). Red data points (flagged for diagenesis by trace element and/or SEM analysis) were excluded from interpretation. If no error bars are visible, the uncertainty is smaller than the size of the symbol. Onset of the main Deccan Traps eruptions (grey dotted line) at 66.413 Ma (Sprain et al., 2019). K-Pg boundary (blue line) at 66.0 Ma. Member names and horizon abbreviations are labeled along right side of figure. Laneye Member is part of underlying Gulpen Formation. *Schiepersberg Member; †Valkenberg Member.
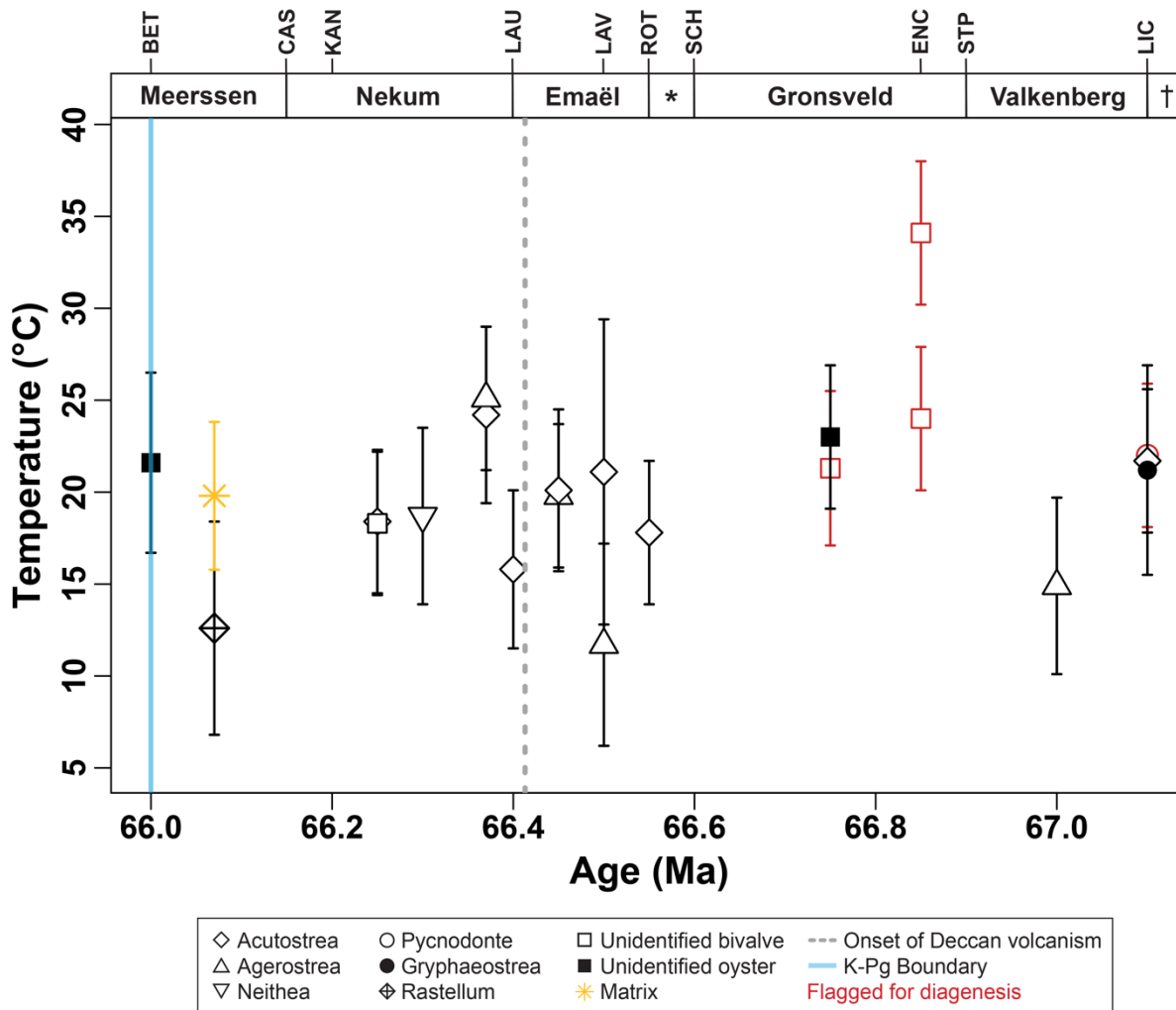
Figure A3: All Δ₄₇-derived paleotemperature data, including samples removed due to diagenesis. Red data points (flagged for diagenesis by trace element and/or SEM analysis) were excluded from interpretation. Both internal and external standard error were calculated for all data points, and the larger of the two errors for each point is depicted here as an error bar. Onset of the main Deccan Traps eruptions (grey dotted line) at 66.413 Ma (Sprain et al., 2019). K-Pg boundary (blue line) at 66.0 Ma. Member names and horizon abbreviations are labeled across the top of the figure. *Schiepersberg Member; †Lanaye Member (of underlying Gulpen Formation).

Table A1: Average paleotemperature data for all Maastrichtian-aged studies reconstructing marine temperatures used to create Figure 6. Data from this study is highlighted in red. All paleolatitudes were determined either directly from each study (if given) or via www.paleolatidude.org (van Hinsbergen et al., 2015).

Study	Proxy type	Locality	Approx. age	Paleolat.	Avg. temp. (°C)
Meyer et al. (2019)	Clumped isotopes of clam, bivalve	North Slope, AK, USA	69.4 Ma	83	7.4
Dennis et al. (2013)	Clumped isotopes of gastropods, nautiloid, ammonites, belemnite, clams	Hell Creek, MT, USA	67.0–73.5 Ma	53	20.5
Tobin et al. (2014)	Clumped isotopes of gastropods, bivalves	Hell Creek, MT, USA	65.2–67.1 Ma	53	25.9
Zhang et al. (2018)	Clumped isotopes of paleosol carbonates	Songliao Basin, China	65.0–76.0 Ma	52	17.0
Meyer et al. (2019)	Clumped isotopes of belemnites, bivalves	Scania, Sweden	69.2–72.3 Ma	46	13.9
Tagliavento et al. (2019)	Clumped isotopes of coccolithic chalk	Danish Basin, Denmark	Late Campanian to Maastrichtian	46	24.5
Maestas et al. (2003)	Planktic foraminiferal $\delta^{18}O$	San Antonio Del Mar, Baja California	Late Campanian to Maastrichtian	42	19.5
Pucéat et al. (2007)	Phosphate $\delta^{18}O$ of fish teeth	Nasilov, Poland	66.0 Ma	40	14.6
Pucéat et al. (2007)	Phosphate $\delta^{18}O$ of fish teeth	South-Central NJ, USA	Mid to late Maastrichtian	40	14.4
This study	Clumped isotopes of oysters, clams, scallops	SE Netherlands & NE Belgium	66.0–67.4 Ma	40	19.2
Vellekoop et al. (2016)	TEX$_{86}$	Monmouth County, NJ, USA	65.6–66.8 Ma	37	26.1
Meyer et al. (2018)	Clumped isotopes of oysters	Monmouth County, NJ, USA	70.7 Ma	37	13.8
Esmeray-Senlet et al. (2015)	Planktic foraminiferal $\delta^{18}O$	Bass River, NJ, USA	66.1–66.6 Ma	36	21.7
Woelders et al. (2018)	Planktic foraminiferal $\delta^{18}O$	Bass River, NJ, USA	66.0–66.3 Ma	36	25.2
Woelders et al. (2018)	TEX$_{86}$	Bass River, NJ, USA	66.1–66.5 Ma	36	27.8
Woelders et al. (2018)	Planktic foraminiferal Mg/Ca	Bass River, NJ, USA	66.1–66.4 Ma	36	22.0
Meyer et al. (2018)	Clumped isotopes of oysters, clams, gastropod	Western TN, USA	73.5 Ma	36	21.5
Vellekoop et al. (2014)	TEX$_{86}$	Brazos River, TX, USA	65.7–66.3 Ma	35	29.8
Meyer et al. (2018)	Clumped isotopes of oysters, clams	Moscow Landing, AL, USA	65.0–74.0 Ma	33	22.1
Meyer et al. (2018)	Clumped isotopes of oysters, clams, belemnite	Burches Ferry, SC, USA	71.4 Ma	33	20.6

Huber et al. (1995)	Planktic foraminiferal $\delta^{18}O$	Blake Nose, North Atlantic Ocean	Maastrichtian	31	18.6
Berggren and Norris (1997)	Planktic foraminiferal $\delta^{18}O$	DSDP 384, North Atlantic Ocean	64.9–66.2 Ma	31	9.8
Frank and Arthur (1999)	Planktic foraminiferal $\delta^{18}O$	Blake Nose, North Atlantic Ocean	Maastrichtian	31	21.1
Huber et al. (2002)	Planktic foraminiferal $\delta^{18}O$	Blake Nose, North Atlantic Ocean	66.0 Ma	31	18.1
Friedrich et al. (2004)	Planktic foraminiferal $\delta^{18}O$	Blake Nose, North Atlantic Ocean	69.6–71.3 Ma	31	19.6
MacLeod et al. (2005)	Planktic foraminiferal $\delta^{18}O$	Blake Nose, North Atlantic Ocean	Late Maastrichtian	31	21.4
Zakharov et al. (2006)	Planktic foraminiferal $\delta^{18}O$	Blake Nose, North Atlantic Ocean	Maastrichtian	31	18.3
Hull et al. (2020)	Bulk carbonate $\delta^{18}O$	IODP U1403, North Atlantic Ocean	66.0–68.8 Ma	31	11.2
Pucéat et al. (2007)	Phosphate $\delta^{18}O$ of fish teeth	Central Morocco	Maastrichtian	21	23.8
MacLeod et al. (2018)	Phosphate $\delta^{18}O$ of teeth	El Kef, Tunisia	65.8–66.4 Ma	21	22.6
Meyer et al. (2019)	Clumped isotopes of oysters, clams	Merced County, CA, USA	69.7–78.0 Ma	21	16.5
Hull et al. (2020)	Bulk and planktic foraminiferal $\delta^{18}O$	ODP 1209, North-West Pacific Ocean	65.8–66.0 Ma	21	18.2
Hull et al. (2020)	Bulk carbonate $\delta^{18}O$	ODP 1209, North-West Pacific Ocean	64.1–66.1 Ma	21	12.4
Meyer et al. (2019)	Clumped isotopes of oysters	Fezzan region, Libya	70.9–71.4 Ma	11	29.2
Li and Keller (1998)	Planktic foraminiferal $\delta^{18}O$	DSDP 525, South Atlantic Ocean	66.0–66.5 Ma	-40	15.0
Kroon et al. (2007)	Bulk carbonate $\delta^{18}O$	ODP 1262, South Atlantic Ocean	65.0–67.1 Ma	-41	9.9
Birch et al. (2016)	Planktic foraminiferal $\delta^{18}O$	ODP 1262, South Atlantic Ocean	66.0–66.5 Ma	-41	14.5
Woelders et al. (2017)	TEX$_{86}$	Bajada del Jagüel, Argentina	64.0–66.7 Ma	-43	27.2
Tobin et al. (2012)	$\delta^{18}O$ of bivalves, gastropods	Seymour Island, Antarctica	65.7–68.5 Ma	-65	8.1
Petersen et al. (2016a)	Clumped isotopes of clams, cockles	Seymour Island, Antarctica	65.8–69.0 Ma	-65	7.7
Stott and Kennett (1990)	Planktic foraminiferal $\delta^{18}O$	ODP 690, South Atlantic Ocean	65.5–68.4 Ma	-70	10.6
Wilf et al. (2003)	Planktic foraminiferal $\delta^{18}O$	ODP 690, South Atlantic Ocean	66.1–66.5 Ma	-70	10.6

Table A2: All data for all samples including SEM results, trace elements, stable and clumped isotopes, paleotemperatures, and δ¹⁸O of seawater. Red samples were excluded from interpretation due to elevated trace element concentrations and/or SEM analysis. Purple samples were excluded from interpretation due to anomalously high δ¹⁸O values. The yellow data are from the matrix sample. In the SEM column, *SG* means secondary growth and *diss* means dissolution.

Sample ID	Site	Strat	Depth (m)	Age (Ma)	Taxa	SEM	Mg (ppm)	Mn (ppm)	Fe (ppm)	δ¹⁸O (‰VPDB)	δ¹⁸O STD	δ¹³C (‰VPDB)	δ¹³C STD	Δ₄₇ (‰VPDB)	Δ₄₇ error	Temp (°C)	Temp error	δ¹⁸Osw (‰VSMOW)	δ¹⁸Osw error
LIC-Psop	ENCI, NL	Lichtenberg Hz	41.45	67.1	psop	NA	1779.67	68.9	1008.85	-1.3	0.04	2.4	0.02						
LIC-Pycn	ENCI, NL	Lichtenberg Hz	41.45	67.1	pycn	SG	4027.37	85.9	4441.3	-1.6	0.1	2.2	0.1	0.698	0.013	22.0	3.9	0.2	0.9
LIC-AcutA	ENCI, NL	Lichtenberg Hz	41.45	67.1	acut	NA	1616.95	37.1	1718.3	-1.5	0.1	2.7	0.1	0.699	0.013	21.7	3.9	0.2	0.9
LIC-Gry	ENCI, NL	Lichtenberg Hz	41.45	67.1	gry	NA	1412.07	41.8	881.5	-1.4	0.2	2.4	0.1	0.701	0.017	21.2	5.7	0.2	1.2
LIC-AcutB	ENCI, NL	Lichtenberg Hz	41.45	67.1	acut	NA	1517.77	44.41	227.93	-1.1	0.1	2.9	0.03						
LIC-Ager	ENCI, NL	Lichtenberg Hz	41.45	67.1	ager	NA	1693.07	59.14	390.33	-1.0	0.02	2.5	0.01						
LIC-Biv	ENCI, NL	Lichtenberg Hz	41.45	67.1	biv	NA	3539.90	89.22	217.45	-1.7	0.04	1.8	0.01						
LIC-Ento	ENCI, NL	Lichtenberg Hz	41.45	67.1	ento	NA	2676.27	88.39	645.54	-2.3	0.01	1.4	0.04						
VAL-Ager	ENCI, NL	Valkenberg Mem	42.5	67.0	ager	NA	2615.75	89.1	1101.6	-1.7	0.2	1.7	0.03	0.720	0.016	14.9	4.8	-1.0	1.1
ENC-Pinna	ENCI, NL	ENCI Hz	44.4	66.85	pinna	NA	3783.09	22.8	475.2	-0.7	0.1	2.6	0.03						
ENC-BivA	ENCI, NL	ENCI Hz	44.4	66.85	biv	NA	4955.74	105.5	4345.3	-1.7	0.1	1.4	0.04	0.692	0.013	24.0	3.9	0.4	0.9
ENC-BivB	ENCI, NL	ENCI Hz	44.4	66.85	biv	diss/SG	4708.41	128	3354.7	-2.0	0.1	1.0	0.1	0.664	0.013	34.1	3.9	2.2	0.9
GRO-Biv	ENCI, NL	Gronsveld Mem	46	66.75	biv	NA	3162.58	210.3	713.0	-1.5	0.02	1.7	0.05	0.700	0.013	21.3	4.2	0.5	0.9
GRO-Ost	ENCI, NL	Gronsveld Mem	46	66.75	oyst	NA	1379.27	55.2	370.5	-1.4	0.1	2.5	0.02	0.695	0.013	23.0	3.9	1.1	0.9
ROT-Acut	ENCI, NL	Romontbos Hz	52.7	66.55	acut	NA	2374.14	50.4	295.1	-1.6	0.1	2.7	0.1	0.710	0.013	17.8	3.9	-0.7	0.9
ROT-Ento	ENCI, NL	Romontbos Hz	52.7	66.55	ento	NA	4576.72	72.7	1032.1	-1.1	0.1	1.6	0.03						
LAV-AcutG	ENCI, NL	Lava Hz	56.75	66.5	acut	NA	1750.24	29.6	597.5	-1.4	0.1	3.2	0.03						
LAV-NeitA	ENCI, NL	Lava Hz	56.75	66.5	neit	NA	2404.16	66.5	3201.1	-1.3	0.1	1.1	0.03						
LAV-NeitB	ENCI, NL	Lava Hz	56.75	66.5	neit	original	2263.15	41.89	711.48	-1.3	0.02	1.6	0.01						
LAV-AcutA	ENCI, NL	Lava Hz	56.75	66.5	acut	NA	3323.55	69.3	1084.3	-0.8	0.1	2.8	0.1	0.704	0.025	21.1	8.3	0.6	1.7
LAV-AcutB	ENCI, NL	Lava Hz	56.75	66.5	acut	original	3073.97	58.8	285.8	-0.7	0.03	3.0	0.02						
LAV-AcutC	ENCI, NL	Lava Hz	56.75	66.5	acut	NA	964.16	23.6	594.9	-1.2	0.1	3.2	0.02						
LAV-AcutD	ENCI, NL	Lava Hz	56.75	66.5	acut	NA	1978.87	60.91	636.42	-1.2	0.04	2.9	0.02						
LAV-AcutE	ENCI, NL	Lava Hz	56.75	66.5	acut	NA	2604.28	47.7	688.9	0.4	0.1	3.6	0.1						
LAV-AcutF	ENCI, NL	Lava Hz	56.75	66.5	acut	NA	3872.70	78.46	95.64	-1.0	0.04	2.4	0.03						
LAV-Ost	ENCI, NL	Lava Hz	56.75	66.5	oyst	NA	3365.03	75.84	599.37	0.7	0.1	3.0	0.04						
LAV-Ager	ENCI, NL	Lava Hz	56.75	66.5	ager	NA	2132.12	49.1	1561.4	-1.1	0.2	2.5	0.1	0.732	0.019	11.7	5.5	-1.6	1.3
LAV-Psop	ENCI, NL	Lava Hz	56.75	66.5	psop	NA	1663.84	48.03	268.6	-1.7	0.1	2.9	0.1						
EMAU-AgerA	ENCI, NL	Emaël Mem	60	66.45	ager	NA	1034.35	36.01	376.01	-1.2	0.04	3.3	0.04						
EMAU-AgerB	ENCI, NL	Emaël Mem	60	66.45	ager	diss/SG	1844.76	40.16	578.15	-1.4	0.1	3.3	0.1						
EMAU-AgerC	ENCI, NL	Emaël Mem	60	66.45	ager	NA	1156.41	40.4	2013.3	-1.4	0.3	3.1	0.2	0.704	0.013	19.8	3.9	-0.1	0.9
EMAU-AcutA	ENCI, NL	Emaël Mem	60	66.45	acut	NA	1032.29	35.1	NA	-1.5	0.2	3.1	0.1	0.704	0.014	20.1	4.4	-0.2	1.0
EMAU-AcutC	ENCI, NL	Emaël Mem	60	66.45	acut	diss	2194.64	60.1	2422.7	-1.0	0.04	2.8	0.02						
EMAU-AcutD	ENCI, NL	Emaël Mem	60	66.45	acut	NA	1195.54	34.84	102.81	-1.4	0.1	2.9	0.01						
EMAU-AcutE	ENCI, NL	Emaël Mem	60	66.45	acut	NA	1880.18	28.4	347.7	-1.3	0.1	3.0	0.04						
EMAU-AcutF	ENCI, NL	Emaël Mem	60	66.45	acut	original	2384.95	58.15	1141.76	-0.5	0.01	3.4	0.01						
EMAU-AgerD	ENCI, NL	Emaël Mem	60	66.45	ager	NA	1815.13	27.87	175.96	-1.3	0.01	3.3	0.01						
EMAU-AcutG	ENCI, NL	Emaël Mem	60	66.45	acut	original	1556.77	37.1	1514.5	-1.5	0.03	3.0	0.02						
EMAU-AcutH	ENCI, NL	Emaël Mem	60	66.45	acut	NA	2127.29	19.23	261.69	-1.3	0.03	4.0	0.01						
EMAU-Cer	ENCI, NL	Emaël Mem	60	66.45	cer	NA	1745.90	35.3	511.9	-0.7	0.01	1.9	0.01						
LAU-Unov	ENCI, NL	Laumont Hz	61.15	66.4	oyst	diss	1953.30	57.04	711.43	-1.3	0.02	3.2	0.02						
LAU-AcutA	ENCI, NL	Laumont Hz	61.15	66.4	acut	NA	2603.99	99.8	7151.1	-0.8	0.1	3.2	0.04						
LAU-AcutB	ENCI, NL	Laumont Hz	61.15	66.4	acut	NA	1947.88	41.91	268.89	-1.3	0.03	3.2	0.02						
LAU-AcutC	ENCI, NL	Laumont Hz	61.15	66.4	acut	NA	887.99	37.9	2007.8	-1.2	0.02	3.2	0.01						
LAU-AcutD	ENCI, NL	Laumont Hz	61.15	66.4	acut	NA	1118.03	47.6	1907.1	-1.0	0.1	3.3	0.01						
LAU-AcutE	ENCI, NL	Laumont Hz	61.15	66.4	acut	original	1222.74	38.55	166.09	-0.7	0.1	3.4	0.04						
LAU-AcutF	ENCI, NL	Laumont Hz	61.15	66.4	acut	NA	727.62	48.6	1014.2	-1.3	0.3	2.8	0.2	0.717	0.014	15.8	4.3	-0.9	1.1
LAU-AcutG	ENCI, NL	Laumont Hz	61.15	66.4	acut	diss	1483.89	36.2	1163.09	-0.9	0.1	3.6	0.02						
NEKB-AcutA	ENCI, NL	Nekum Mem (base)	62	66.37	acut	NA	1169.96	24.6	724.2	-1.1	0.01	3.3	0.003	0.691	0.016	24.2	4.8	1.2	1.1
NEKB-AcutBC	ENCI, NL	Nekum Mem (base)	62	66.37	acut	original	1769.21	35.95	248.56	-1.2	0.1	3.3	0.1						
NEKB-AcutD	ENCI, NL	Nekum Mem (base)	62	66.37	acut	diss	1365.33	16.66	225.46	-1.5	0.1	3.5	0.1						
NEKB-AcutE	ENCI, NL	Nekum Mem (base)	62	66.37	acut	diss	2481.96	41.9	2068.5	-0.9	0.03	2.7	0.04						
NEKB-AcutF	ENCI, NL	Nekum Mem (base)	62	66.37	acut	NA	2174.63	46.2	3608.6	-0.5	0.02	2.8	0.01						
NEKB-Ager	ENCI, NL	Nekum Mem (base)	62	66.37	ager	NA	1981.93	59.8	386.7	-1.4	0.1	2.6	0.03	0.689	0.013	25.1	3.9	1.0	0.9
NEK-Neit	ENCI, NL	Nekum Mem (mid)	64	66.3	neit	diss/SG	2677.14	45.53	435.82	-1.4	0.1	1.8	0.1						
NEK-NeitB	ENCI, NL	Nekum Mem (mid)	64	66.3	neit	NA	2122.18	38.9	285.8	-1.6	0.1	1.6	0.04	0.708	0.016	18.7	4.8	-0.1	1.1
CBR-Acut	CBR, BE	Nekum Mem (CBR)	65	66.25	acut	NA	2361.67	31.1	482.2	-2.1	0.1	2.8	0.04	0.709	0.013	18.4	3.9	-0.6	0.9
CBR-Biv	CBR, BE	Nekum Mem (CBR)	65	66.25	biv	NA	2291.73	21.4	225.5	-1.2	0.1	3.1	0.03	0.709	0.013	18.3	3.9	0.2	0.9
MEER-RasB	ENCI, NL	Meerssen Mem	76	66.07	ras	original	1194.89	34.8	843.0	-1.4	0.1	2.1	0.1	0.729	0.020	12.6	5.8	-1.8	1.3
MEER-mat	ENCI, NL	Meerssen Mem	76	66.07	mat	NA	5886.04	60.24	664.19	-0.3	0.1	1.3	0.04	0.705	0.013	19.8	4.0	1.0	0.9
GCAV-OystA	GSGs, NL	Berg en Terbljit Hz	85	66.0	oyst	original	861.60	60.82	245.33	-2.5	0.1	2.7	0.02	0.699	0.013	21.6	4.9	-0.8	0.9

REFERENCES

Barnet, J. S. K., Littler, K., Westerhold, T., Kroon, D., Leng, M. J., Bailey, I., Röhl, U., and Zachos, J. C.: A High-fidelity benthic stable isotope record of Late Cretaceous–Early Eocene climate change and carbon-cycling, Paleoceanogr. Paleoclimatol., 34, 672–691, https://doi.org/10.1029/2019PA003556, 2019.

Bernasconi, S. M., Daëron, M., Bergmann, K. D., Bonifacie, M., Meckler, A. N., Affek, H. P., et al.: InterCarb: A community effort to improve interlaboratory standardization of the carbonate clumped isotope thermometer using carbonate standards. Geochem., Geophy., Geosy., 22, https://doi.org/10.1029/2020GC009588, 2021.

Bless, M. J. M.: Possible causes for the change in ostracod assemblages at the Maastrichtian-Palaeocene boundary in southern Limburg, The Netherlands, Meded. Werkgr. Tert. Kwart. Geol., 25, 197–211, 1988.

Bowman, V. C., Riding, J. B., Francis, J. E., Crame, J. A., and Hannah, M. J.: The taxonomy and palaeobiogeography of small chorate dinoflagellate cysts from the Late Cretaceous to Quaternary of Antarctica, Palynology, 37, 151–169, https://doi.org/10.1080/01916122.2012.750898, 2013.

Brand, U. and Morrison, J. O.: Biogeochemistry of fossil marine invertebrates. Geosci. Can., 14, 1987.

Brinkhuis, H. and Schiøler, P.: Palynology of the Geulhemmerberg Cretaceous/Tertiary boundary section (Limburg, SE Netherlands), Geol. Mijnbouw, 75, 193–213, 1996.

Bush, A. B. G. and Philander, S. G. H.: The Late Cretaceous: Simulation with a coupled atmosphere-ocean general circulation model, Paleoceanography, 12, 495–516, https://doi.org/10.1029/97PA00721, 1997.

Came, R. E., Brand, U., and Affek, H. P.: Clumped isotope signatures in modern brachiopod carbonate, Chem. Geol., 377, 20–30, https://doi.org/10.1016/j.chemgeo.2014.04.004, 2014.

Clyde, W. C., Ramezani, J., Johnson, K. R., Bowring, S. A., and Jones, M. M.: Direct high-precision U–Pb geochronology of the end-Cretaceous extinction and calibration of Paleocene astronomical timescales, Earth Planet. Sci. Lett., 452, 272–280, https://doi.org/10.1016/j.epsl.2016.07.041, 2016.

de Winter, N. J. D., Vellekoop, J., Vorsselmans, R., Golreihan, A., Soete, J., Petersen, S. V., Meyer, K. W., Casadio, S., Speijer, R. P., Claeys, P.: An assessment of latest Cretaceous Pycnodonte vesicularis (Lamarck, 1806) shells as records for palaeoseasonality: a multi-proxy investigation, Clim. Past, 14, 725–749, https://doi.org/10.5194/cp-14-725-2018, 2018.

Defliese, W. F., Hren, M. T., and Lohmann, K. C.: Compositional and temperature effects of phosphoric acid fractionation on Δ_{47} analysis and implications for discrepant calibrations, Chem. Geol., 396, 51–60, https://doi.org/10.1016/j.chemgeo.2014.12.018, 2015.

Dennis, K. J., Affek, H. P., Passey, B. H., Schrag, D. P., and Eiler, J. M.: Defining an absolute reference frame for 'clumped' isotope studies of CO_2, Geochim. Cosmochim. Ac., 75, 7117–7131, https://doi.org/10.1016/j.gca.2011.09.025, 2011.

Dennis, K. J., Cochran, J. K., Landman, N. H., and Schrag, D. P.: The climate of the Late Cretaceous: New insights from the application of the carbonate clumped isotope thermometer to Western Interior Seaway macrofossil, Earth Planet. Sci. Lett., 362, 51–65, https://doi.org/10.1016/j.epsl.2012.11.036, 2013.

Dortangs, R. W., Schulp, A. S., Mulder, E. W., Jagt, J. W., Peeters, H. H., and De Graaf, D. T.: A large new mosasaur from the Upper Cretaceous of The Netherlands, Neth. J. Geosci., 81, 1–8, https://doi.org/10.1017/S0016774600020515, 2002.

Dusar, M. and Lagrou, D.: Cretaceous flooding of the Brabant Massif and the lithostratigraphic characteristics of its chalk cover in northern Belgium, Geol. Belg., 10, 27–38, 2007.

Eagle, R. A., Eiler, J. M., Tripati, A. K., Ries, J. B., Freitas, P. S., Hiebenthal, C., Wanamaker Jr, A. D., Taviani, M., Elliot, M., and Marenssi, S.: The influence of temperature and seawater carbonate saturation state on ^{13}C–^{18}O bond ordering in bivalve mollusks, Biogeosciences, 10, 4591–4606, https://doi.org/10.5194/bg-10-4591-2013, 2013.

Eide, M., Olsen, A., Ninnemann, U. S., and Johannessen, T.: A global ocean climatology of preindustrial and modern ocean $\delta^{13}C$, Global Biogeochem. Cy., 31, 515–534, https://doi.org/10.1002/2016GB005472, 2017.

Eiler, J. M.: Paleoclimate reconstruction using carbonate clumped isotope thermometry, Quaternary Sci. Rev., 30, 3575–3588, https://doi.org/10.1016/j.quascirev.2011.09.001, 2011.

Engelke, J., Linnert, C., Mutterlose, J., and Wilmsen, M.: Early Maastrichtian benthos of the chalk at Kronsmoor, northern Germany: implications for Late Cretaceous environmental change, Palaeobio. Palaeoenv., 97, 703–722, https://doi.org/10.1007/s12549-017-0283-2, 2017.

Felder, W. M.: Lithostratigrafie van het Boven-Krijt en het Dano-Montien in Zuid-Limburg en het aangrenzende gebied, Rijks Geologische Dienst (Haarlem), 63–72, 1975.

Fendley, I. M., Mittal, T., Sprain, C. J., Marvin-DiPasquale, M., Tobin, T. S., and Renne, P. R.: Constraints on the volume and rate of Deccan Traps flood basalt eruptions using a combination of high-resolution terrestrial mercury records and geochemical box models, Earth Planet. Sci. Lett., 524, https://doi.org/10.1016/j.epsl.2019.115721, 2019.

Font, E., Adatte, T., Sial, A. N., de Lacerda, L. D., Keller, G., and Punekar, J.: Mercury anomaly, Deccan volcanism, and the end-Cretaceous mass extinction, Geology, 44, 171–174, https://doi.org/10.1130/G37451.1, 2016.

Gale, A. S. and Christensen, W. K.: Occurrence of the belemnite Actinocamax plenus in the, B. Geol. Soc. Denmark, 43, 68–77, 1996.

Gao, Y., Ibarra, D. E., Rugenstein, J. K. C., Chen, J., Kukla, T., Methner, K., Gao, Y., Huang, H., Lin, Z., and Zhang, L.: Terrestrial climate in mid-latitude East Asia from the latest Cretaceous to the earliest Paleogene: A multiproxy record from the Songliao Basin in northeastern China, Earth-Sci. Rev., 216, https://doi.org/10.1016/j.earscirev.2021.103572, 2021.

Golovneva, L. B.: The Maastrichtian (Late Cretaceous) climate in the northern hemisphere, Geol. Soc. London Spec. Publ., 181, 43–54, https://doi.org/10.1144/GSL.SP.2000.181.01.05, 2000.

Haq, B. U.: Cretaceous eustasy revisited, Global Planet. Change, 113, 44–58, https://doi.org/10.1016/j.gloplacha.2013.12.007, 2014.

Hart, M. B., FitzPatrick, M. E., and Smart, C. W.: The Cretaceous/Paleogene boundary: Foraminifera, sea grasses, sea level change and sequence stratigraphy, Palaeogeogr. Palaeocl., 441, 420–429, https://doi.org/10.1016/j.palaeo.2015.06.046, 2016.

Henkes, G. A., Passey, B. H., Wanamaker Jr, A. D., Grossman, E. L., Ambrose Jr, W. G., and Carroll, M. L.: Carbonate clumped isotope compositions of modern marine mollusk and brachiopod shells, Geochim. Cosmochim. Ac., 106, 307–325, https://doi.org/10.1016/j.gca.2012.12.020, 2013.

Henkes, G. A., Passey, B. H., Grossman, E. L., Shenton, B. J., Pérez-Huerta, A., and Yancey, T. E.: Temperature limits for preservation of primary calcite clumped isotope paleotemperatures, Geochim. Cosmochim, Ac., 139, 362–382, https://doi.org/10.1016/j.gca.2014.04.040, 2014.

Hull, P. M., Bornemann, A., Penman, D. E., Henehan, M. J., Norris, R. D., Wilson, P. A., Blum, P., Alegret, L., Batenburg, S. J., and Bown, P. R.: On impact and volcanism across the Cretaceous-Paleogene boundary, Science, 367, 266–272, https://doi.org/10.1126/science.aay5055, 2020.

Jagt, J. W. M. and Jagt-Yazykova, E. A.: Stratigraphy of the type Maastrichtian–a synthesis, Scripta Geologica Special Issue, 8, 5–32, 2012.

Jagt, J. W., Donovan, S. K., Fraaije, R., Mulder, E. W., Nieuwenhuis, E., Stroucken, J., van Bakel, B., and van Knippenberg, P.: Remarkable preservation of selected latest Cretaceous macrofossils from the Maastrichtian type area (the Netherlands, Belgium), Fossil Record 4: Bulletin, 67, 75, 2016.

Keutgen, N.: A bioclast-based astronomical timescale for the Maastrichtian in the type area (southeast Netherlands, northeast Belgium) and stratigraphic implications: the legacy of PJ Felder, Neth. J. Geosci., 97, 229–260, https://doi.org/10.1017/njg.2018.15, 2018.

Kim, S. T. and O'Neil, J. R.: Equilibrium and nonequilibrium oxygen isotope effects in synthetic carbonates, Geochim. Cosmochim. Ac., 61, 3461–3475, https://doi.org/10.1016/S0016-7037(97)00169-5, 1997.

Kodama, K. P. and Ward, P. D.: Compaction-corrected paleomagnetic paleolatitudes for Late Cretaceous rudists along the Cretaceous California margin: Evidence for less than 1500 km of post–Late Cretaceous offset for Baja British Columbia, Geol. Soc. Am. Bull., 113, 1171–1178, https://doi.org/10.1130/0016-7606(2001)113%3C1171:CCPPFL%3E2.0.CO;2, 2001.

Ladant, J. B. and Donnadieu, Y.: Palaeogeographic regulation of glacial events during the Cretaceous supergreenhouse, Nat. Commun., 7, 1–9, https://doi.org/10.1038/ncomms12771, 2016.

Ladant, J. B., Poulsen, C. J., Fluteau, F., Tabor, C. R., MacLeod, K. G., Martin, E. E., Haynes, S. J., and Rostami, M. A.: Paleogeographic controls on the evolution of Late Cretaceous ocean circulation, Clim. Past, 16, 973–1006, https://doi.org/10.5194/cp-16-973-2020, 2020.

Land, L. S.: Diagenesis of skeletal carbonates, J. Sediment Res., 37, 914–930, https://doi.org/10.1306/74D717D5-2B21-11D7-8648000102C1865D, 1967.

Leloux, J.: Numerical distribution of Santonian to Danian corals (Scleractinia, Octocorallia) of southern Limburg, the Netherlands, Geol. Mijnbouw, 78, 191–195, https://doi.org/10.1023/A:1003743301625, 1999.

Li, L. and Keller, G.: Abrupt deep-sea warming at the end of the Cretaceous, Geology, 26, 995–998, https://doi.org/10.1130/0091-7613(1998)026%3C0995:ADSWAT%3E2.3.CO;2, 1998.

Liebau, A.: Paläobathymetrische und paläoklimatische Veränderungen im Mikrofaunenbild der Maastrichter Tuffkreide, Neues Jahrb. Geol. P. A., 157, 233–237, 1978.

Luijendijk, E., Van Balen, R. T., Ter Voorde, M., and Andriessen, P. A. M.: Reconstructing the Late Cretaceous inversion of the Roer Valley Graben (southern Netherlands) using a new model that integrates burial and provenance history with fission track thermochronology, J. Geophys. Res.-Sol. Ea., 116, https://doi.org/10.1029/2010JB008071, 2011.

Maastricht Climate: https://en.climate-data.org/europe/the-netherlands/limburg/maastricht-893/#temperature-graph, last access: 14 June 2021.

Meyer, K. W., Petersen, S. V., Lohmann, K. C., and Winkelstern, I. Z.: Climate of the Late Cretaceous North American Gulf and Atlantic Coasts, Cretaceous Res., 89, 160–173, https://doi.org/10.1016/j.cretres.2018.03.017, 2018.

Meyer, K. W., Petersen, S. V., Lohmann, K. C., Blum, J. D., Washburn, S. J., Johnson, M. W., Gleason, J. D., Kurz, A. Y., and Winkelstern, I. Z.: Biogenic carbonate mercury and marine temperature records reveal global influence of Late Cretaceous Deccan Traps, Nat. Commun., 10, 1–8, https://doi.org/10.1038/s41467-019-13366-0, 2019.

Miller, K. G., Wright, J. D., and Browning, J. V.: Visions of ice sheets in a greenhouse world, Mar. Geol., 217, 215–231, https://doi.org/10.1016/j.margeo.2005.02.007, 2005.

Molina, E., Alegret, L., Arenillas, I., Arz, J. A., Gallala, N., Hardenbol, J., Salis, K. von, Steurbaut, E., Vandenberghe, N., and Zaghbib-Turki, D.: The global boundary stratotype section and point for the base of the Danian stage (Paleocene, Paleogene," Tertiary", Cenozoic) at El Kef, Tunisia-original definition and revision, Episodes, 29, 263–273, 2006.

Möller, P. and Kubanek, F.: Role of magnesium in nucleation processes of calcite, aragonite and dolomite, Neues Jb. Miner. Abh., 126, 199–220, 1976.

Nava, A. H., Black, B. A., Gibson, S. A., Bodnar, R. J., Renne, P. R., and Vanderkluysen, L.: Reconciling early Deccan Traps CO_2 outgassing and pre-KPB global climate, P. Natl. Acad. Sci. USA, 118, https://doi.org/10.1073/pnas.2007797118, 2021.

Percival, L. M., Jenkyns, H. C., Mather, T. A., Dickson, A. J., Batenburg, S. J., Ruhl, M., Hesselbo, S. P., Barclay, R., Jarvis, I., and Robinson, S. A.: Does large igneous province volcanism always perturb the mercury cycle? Comparing the records of Oceanic Anoxic Event 2 and the end-Cretaceous to other Mesozoic events, Am. J. Sci., 318, 799–860, https://doi.org/10.2475/08.2018.01, 2018.

Petersen, S. V., Dutton, A., and Lohmann, K. C.: End-Cretaceous extinction in Antarctica linked to both Deccan volcanism and meteorite impact via climate change, Nat. Commun., 7, 1–9, https://doi.org/10.1038/ncomms12079, 2016a.

Petersen, S. V., Tabor, C. R., Lohmann, K. C., Poulsen, C. J., Meyer, K. W., Carpenter, S. J., Erickson, J. M., Matsunaga, K. K., Smith, S. Y., and Sheldon, N. D.: Temperature and salinity of the Late Cretaceous western interior seaway, Geology, 44, 903–906, https://doi.org/10.1130/G38311.1, 2016b.

Petersen, S. V., Winkelstern, I. Z., Lohmann, K. C., and Meyer, K. W.: The effects of Porapak^{TM} trap temperature on $\delta^{18}O$, $\delta^{13}C$, and Δ_{47} values in preparing samples for clumped isotope analysis, Rapid Commun. Mass Sp., 30, 199–208, https://doi.org/10.1002/rcm.7438, 2016c.

Petersen, S. V., Defliese, W. F., Saenger, C., Daëron, M., Huntington, K. W., John, C. M., Kelson, J. R., Bernasconi, S. M., Colman, A. S., and Kluge, T.: Effects of improved ^{17}O correction on interlaboratory agreement in clumped isotope calibrations, estimates of mineral-specific offsets, and temperature dependence of acid digestion fractionation, Geochem., Geophy., Geosy., 20, 3495–3519, https://doi.org/10.1029/2018GC008127, 2019.

Pucéat, E., Lécuyer, C., Donnadieu, Y., Naveau, P., Cappetta, H., Ramstein, G., Huber, B. T., and Kriwet, J.: Fish tooth $\delta^{18}O$ revising Late Cretaceous meridional upper ocean water temperature gradients, Geology, 35, 107–110, https://doi.org/10.1130/G23103A.1, 2007.

Ravizza, G. and Peucker-Ehrenbrink, B.: Chemostratigraphic evidence of Deccan volcanism from the marine osmium isotope record, Science, 302, 1392–1395, https://doi.org/10.1126/science.1089209, 2003.

Remin, Z., Gruszczyński, M., and Marshall, J. D.: Changes in paleo-circulation and the distribution of ammonite faunas at the Coniacian–Santonian transition in central Poland and western Ukraine, Acta Geol. Pol., 66, https://doi.org/10.1515/agp-2016-0006, 2016.

Schiøler, P., Brinkhuis, H., Roncaglia, L., and Wilson, G. J.: Dinoflagellate biostratigraphy and sequence stratigraphy of the type Maastrichtian (Upper Cretaceous), ENCI Quarry, The Netherlands, Mar. Micropaleontol., 31, 65–95, https://doi.org/10.1016/S0377-8398(96)00058-8, 1997.

Schulte, P., Alegret, L., Arenillas, I., Arz, J. A., Barton, P. J., Bown, P. R., Bralower, T. J., Christeson, G. L., Claeys, P., and Cockell, C. S.: The Chicxulub asteroid impact and mass extinction at the Cretaceous-Paleogene boundary, Science, 327, 1214–1218, https://doi.org/10.1126/science.1177265, 2010.

Scotese, C. R.: An Atlas of Phanerozoic Paleogeographic Maps: The Seas Come In and the Seas Go Out, Annu. Rev. Earth Pl. Sc., 49, 669–718, https://doi.org/10.1146/annurev-earth-081320-064052, 2021.

Sial, A. N., Chen, J., Lacerda, L. D., Frei, R., Tewari, V. C., Pandit, M. K., Gaucher, C., Ferreira, V. P., Cirilli, S., and Peralta, S.: Mercury enrichment and Hg isotopes in Cretaceous–Paleogene boundary successions: Links to volcanism and palaeoenvironmental impacts, Cretaceous Res., 66, 60–81, https://doi.org/10.1016/j.cretres.2016.05.006, 2016.

Smit, J.: The global stratigraphy of the Cretaceous-Tertiary boundary impact ejecta, Annu. Rev. Earth Pl. Sc., 27, 75–113, https://doi.org/10.1146/annurev.earth.27.1.75, 1999.

Smit, J. and Brinkhuis, H.: The Geulhemmerberg Cretaceous/Tertiary boundary section (Maastrichtian type area, SE Netherlands); summary of results and a scenario of events. Geol. Mijnbouw, 75, 283–293, 1996.

Sprain, C. J., Renne, P. R., Clemens, W. A., and Wilson, G. P.: Calibration of chron C29r: New high-precision geochronologic and paleomagnetic constraints from the Hell Creek region, Montana, Geol. Soc. Am. Bull., 130, 1615–1644, https://doi.org/10.1130/B31890.1, 2018.

Sprain, C. J., Renne, P. R., Vanderkluysen, L., Pande, K., Self, S., and Mittal, T.: The eruptive tempo of Deccan volcanism in relation to the Cretaceous-Paleogene boundary, Science, 363, 866–870, https://doi.org/10.1126/science.aav1446, 2019.

Stott, L. D. and Kennett, J. P.: The paleoceanographic and paleoclimatic signature of the Cretaceous/Paleogene boundary in the Antarctic: stable isotopic results from ODP Leg 113, in: Proceedings of the Ocean Drilling Program, Scientific Results, 113, 829–848, 1990.

Tabor, C. R., Poulsen, C. J., Lunt, D. J., Rosenbloom, N. A., Otto-Bliesner, B. L., Markwick, P. J., Brady, E. C., Farnsworth, A., and Feng, R.: The cause of Late Cretaceous cooling: A multimodel-proxy comparison, Geology, 44, 963–966, https://doi.org/10.1130/G38363.1, 2016.

Tagliavento, M., John, C. M., and Stemmerik, L.: Tropical temperature in the Maastrichtian Danish Basin: Data from coccolith Δ_{47} and $\delta^{18}O$, Geology, 47, 1074–1078, https://doi.org/10.1130/G46671.1, 2019.

Tobin, T. S., Ward, P. D., Steig, E. J., Olivero, E. B., Hilburn, I. A., Mitchell, R. N., Diamond, M. R., Raub, T. D., and Kirschvink, J. L.: Extinction patterns, $\delta^{18}O$ trends, and magnetostratigraphy from a southern high-latitude Cretaceous–Paleogene section: Links with Deccan volcanism, Palaeogeogr. Palaeocl., 350, 180–188, https://doi.org/10.1016/j.palaeo.2012.06.029, 2012.

Tobin, T. S., Wilson, G. P., Eiler, J. M., and Hartman, J. H.: Environmental change across a terrestrial Cretaceous-Paleogene boundary section in eastern Montana, USA, constrained by carbonate clumped isotope paleothermometry, Geology, 42, 351–354, https://doi.org/10.1130/G35262.1, 2014.

Tobin, T. S., Bitz, C. M., and Archer, D.: Modeling climatic effects of carbon dioxide emissions from Deccan Traps volcanic eruptions around the Cretaceous–Paleogene boundary, Palaeogeogr. Palaeocl., 478, 139–148, https://doi.org/10.1016/j.palaeo.2016.05.028, 2017.

Ullmann, C. V., Campbell, H. J., Frei, R., Hesselbo, S. P., Pogge von Strandmann, P. A. E., and Korte, C.: Partial diagenetic overprint of Late Jurassic belemnites from New Zealand: Implications for the preservation potential of δ^7Li values in calcite fossils, Geochim. Cosmochim. Ac., 120, 80–96, https://doi.org/10.1016/j.gca.2013.06.029, 2013.

Vandenberghe, N., Craen, M. D., and Beerten, K.: Geological framework of the Campine Basin, SCK• CEN, 112, 2014.

van der Ham, R. W. J. M., van Konijnenburg-van Cittert, J. H. A., Jagt, J. W. M., Indeherberge, L., Meuris, R., Deckers, M. J. M., Renkens, S., and Laffineur, J.: Seagrass stems with attached roots from the type area of the Maastrichtian Stage (NE Belgium, SE Netherlands): Morphology, anatomy, and ecological aspects, Rev. Palaeobot. and Palyno., 241, 49–69, https://doi.org/10.1016/j.revpalbo.2017.02.001, 2017.

van Hinsbergen, D. J., de Groot, L. V., van Schaik, S. J., Spakman, W., Bijl, P. K., Sluijs, A., Langereis, C. G., and Brinkhuis, H.: A paleolatitude calculator for paleoclimate studies. PloS ONE, 10, 2015.

Vellekoop, J., Sluijs, A., Smit, J., Schouten, S., Weijers, J. W. H., Sinninghe Damste, J. S., and Brinkhuis, H.: Rapid short-term cooling following the Chicxulub impact at the Cretaceous-Paleogene boundary, Proceedings of the National Academy of Sciences, P. Natl. Acad. Sci. USA, 111, 7537–7541, https://doi.org/10.1073/pnas.1319253111, 2014.

Vellekoop, J., Esmeray-Senlet, S., Miller, K. G., Browning, J. V., Sluijs, A., Schootbrugge, B. van de, Damsté, J. S. S., and Brinkhuis, H.: Evidence for Cretaceous-Paleogene boundary bolide "impact winter" conditions from New Jersey, USA, Geology, 44, 619–622, https://doi.org/10.1130/G37961.1, 2016.

Vellekoop, J., Sluijs, A., Speijer, R.P.: An acme of the dinoflagellate cyst Palynodinium grallator, Gocht, 1970; a marker for the late Maastrichtian warming event at Northern mid-latitudes?, Geol. Belg. [accepted manuscript], 2018.

Vellekoop, J., Woelders, L., Sluijs, A., Miller, K. G., and Speijer, R. P.: Phytoplankton community disruption caused by latest Cretaceous global warming, Biogeosciences, 16, 4201–4210, https://doi.org/10.5194/bg-16-4201-2019, 2019.

Vellekoop, J., van Tilborgh, K. H. V., Knippenberg, P. V., Jagt, J. W. M., Stassen, P., Goolaerts, S., and Speijer, R. P.: Type-Maastrichtian gastropod faunas show rapid ecosystem recovery following the Cretaceous–Palaeogene boundary catastrophe, Palaeontology, 63, 349–367, https://doi.org/10.1111/pala.12462, 2020.

Vellekoop, J., Kaskes, P., Sinnesael, M., Dehais, T., Huygh, J., Jagt, J., Speijer, R. P., Claeys, P.: A new chemostratigraphic framework for the Maastrichtian type area (southeastern Netherlands, northeastern Belgium), in prep.

Voigt, S., Wilmsen, M., Mortimore, R. N., Voigt, T.: Cenomanian palaeotemperatures derived from the oxygen isotopic composition of brachiopods and belemnites: evaluation of Cretaceous palaeotemperature proxies. Int. J. Earth Sci., 92, 285–299, https://doi.org/10.1007/s00531-003-0315-1, 2003.

Watkins, D. K. and Self-Trail, J. M.: Calcareous nannofossil evidence for the existence of the Gulf Stream during the late Maastrichtian, Paleoceanography, 20, https://doi.org/10.1029/2004PA001121, 2005.

Wilf, P., Johnson, K. R., and Huber, B. T.: Correlated terrestrial and marine evidence for global climate changes before mass extinction at the Cretaceous-Paleogene boundary, P. Natl. Acad. Sci. USA, 100, 599–604, https://doi.org/10.1073/pnas.0234701100, 2003.

Winkelstern, I. Z. and Lohmann, K. C.: Shallow burial alteration of dolomite and limestone clumped isotope geochemistry, Geology, 44, 467–470, https://doi.org/10.1130/G37809.1, 2016.

Woelders, L., Vellekoop, J., Kroon, D., Smit, J., Casadío, S., Prámparo, M. B., Dinarès-Turell, J., Peterse, F., Sluijs, A., Lenaerts, J. T. M., and Speijer, R. P.: Latest Cretaceous climatic and environmental change in the South Atlantic region, Paleoceanography, 32, 466–483, https://doi.org/10.1002/2016PA003007, 2017.

Woelders, L., Vellekoop, J., Weltje, G. J., de Nooijer, L., Reichart, G.-J., Peterse, F., Claeys, P., and Speijer, R. P.: Robust multi-proxy data integration, using late Cretaceous paleotemperature records as a case study, Earth Planet. Sci. Lett., 500, 215–224, https://doi.org/10.1016/j.epsl.2018.08.010, 2018.

Zhang, L., Wang, C., Wignall, P. B., Kluge, T., Wan, X., Wang, Q., and Gao, Y.: Deccan volcanism caused coupled pCO2 and terrestrial temperature rises, and pre-impact extinctions in northern China, Geology, 46, 271–274, https://doi.org/10.1130/G39992.1, 2018.

Zhang, J. Z., Petersen, S. V., Winkelstern, I. Z., Lohmann, K. C.: Seasonally variable aquifer discharge and cooler climate in Bermuda during the Last Interglacial revealed by subannual clumped isotope analysis, Paleoceanogr. Paleoclimatol. [accepted manuscript], https://doi.org/10.1029/2020PA004145, 2021.

Zhao, M., Ma, M., He, M., Qiu, Y., Liu, X.: Evaluation of the four potential Cretaceous-Paleogene (K-Pg) boundaries in the Nanxiong Basin based on evidences from volcanic activity and paleoclimatic evolution, Sci. China Earth Sci., 64, 631–641, https://doi.org/10.1007/s11430-020-9736-0, 2021.

Zijlstra, J. J. P.: The sedimentology of upper Maastrichtian shelf carbonates in quarry ENCI (Maastricht, The Netherlands). 9th IAS Regional Meeting, Belgium, Excursion Guide 29 [unpublished], 1988.

Zijlstra, J. J. P.: Sedimentology of the Late Cretaceous and Early Tertiary (tuffaceous) chalk of northwest Europe, PhD thesis, Utrecht University, Netherlands, 184 pp., ISBN 90-71577-73-2, 1994.